Stable Rechargeable Aqueous Zinc Ion Battery Achieved by Cation Deficient Cathode Material and Gelatin Modified Separator

by

Shengkai Li

A thesis

presented to the University of Waterloo

in fulfillment of the

thesis requirement for the degree of

Master of Applied Science

in

Chemical Engineering

Waterloo, Ontario, Canada, 2019

© Shengkai Li

AUTHOR'S DECLARATION

I hereby declare that I am the sole author of this thesis. This is a true copy of the thesis, including any required final revisions, as accepted by my examiners.

I understand that my thesis may be made electronically available to the public.

Abstract

The widespread utilization of renewable and clean energy sources like solar, wind and biomass energy inspires the energy storage market, and a stable, cost-effective and environmentally friendly energy storage system is the key to this demand. Aqueous rechargeable lithium ion batteries (ARLIBs), rechargeable hybrid aqueous batteries (ReHABs) and aqueous zinc ion batteries (ZIBs) are competitive candidates for their advantages of being safe, environmentally friendly and of higher ionic conductivity. For material abundance, low cost and multivalent charge transport, ZIBs are more attractive.

In this research, manganese deficient zinc manganese oxide was synthesized by oxidation-precipitation with different zinc and manganese ratio. The cathode material synthesized with 1:3 zinc to manganese ratio has the highest initial capacity and also best rate performance. The exact chemical formula for the ZMO sample is $ZnMn_{1.71}O_4$, which calculated by the XPS results. The abundant of manganese vacancies also promotes high zinc diffusivity. The zinc diffusion coefficient of the $ZnMn_{1.71}O_4$ is 4.44E-11cm^2/s, which is comparable with the Li diffusion coefficient normally at a magnitude of $\sim 10^{-10}$cm^2/s in spinel cathode. However, the capacity retention is only 33.5% after 500 cycles with the 300mA·g^{-1} current density.

Then, gelatin modified separator was introduced into the battery system to prolong the battery cycle life. The capacity retention achieves 91.3% after 500 cycles at the current density of 300mA·g^{-1}, which is an unimaginable improvement. Moreover, 7mAh large battery was used for simulating the industrial situation with extensive cathode mass loading. The capacity remains 80% after 2000cycles at 500mA·g^{-1} current density. Zinc to zinc symmetric cell was applied for

simulating the dendrite growth during the cycling. The symmetric cell with G-AGM can keep ruing for five days without evident voltage increasing. However, the symmetric cells without G-AGM stop running on the third day due to the voltage is excess the limitation. The result of CA test and the SEM images of the zinc electrodes after CA test are all the evidence that can prove that G-AGM has a strong effect on inhibiting zinc dendrite nucleation and growth.

Acknowledgements

I would like to acknowledge my supervisor, Prof. Pu Chen, for the wonderful opportunity to pursue my graduate studies and for his continuous guidance and support during this period.

I would also like to thank lab colleagues including Dr Jian Zhi, Dr Yu Liu, Mei Han, Zhimou Yu for their assistance and support.

I would also like to acknowledge my reading committee members Prof. Yuning Li and Prof. Michael Fowler for their time and constructive feedback towards the completion of this thesis.

At the last, I would like to thank my parents and my sisters for their love and support throughout the master's program.

Table of Contents

List of Figures

List of Tables

Chapter 1: Introduction

1.1 Introduction

Due to the global energy crisis and climate change, developing renewable and environmentally friendly energy sources is a suitable solution for every country. Figure 1 shows the trends of installed renewable energy capacity from 2010 to 2018. In 2010, the total renewable energy capacity was only about 1200KMW, but it achieves 2300KMW in 2018, which almost doubled. The increasing trends of renewable energy capacity also lead to the growing demand for battery energy storage systems (BESS) which can help make renewable energy — whose power output cannot be controlled by grid operators — smooth and dispatchable. [2]
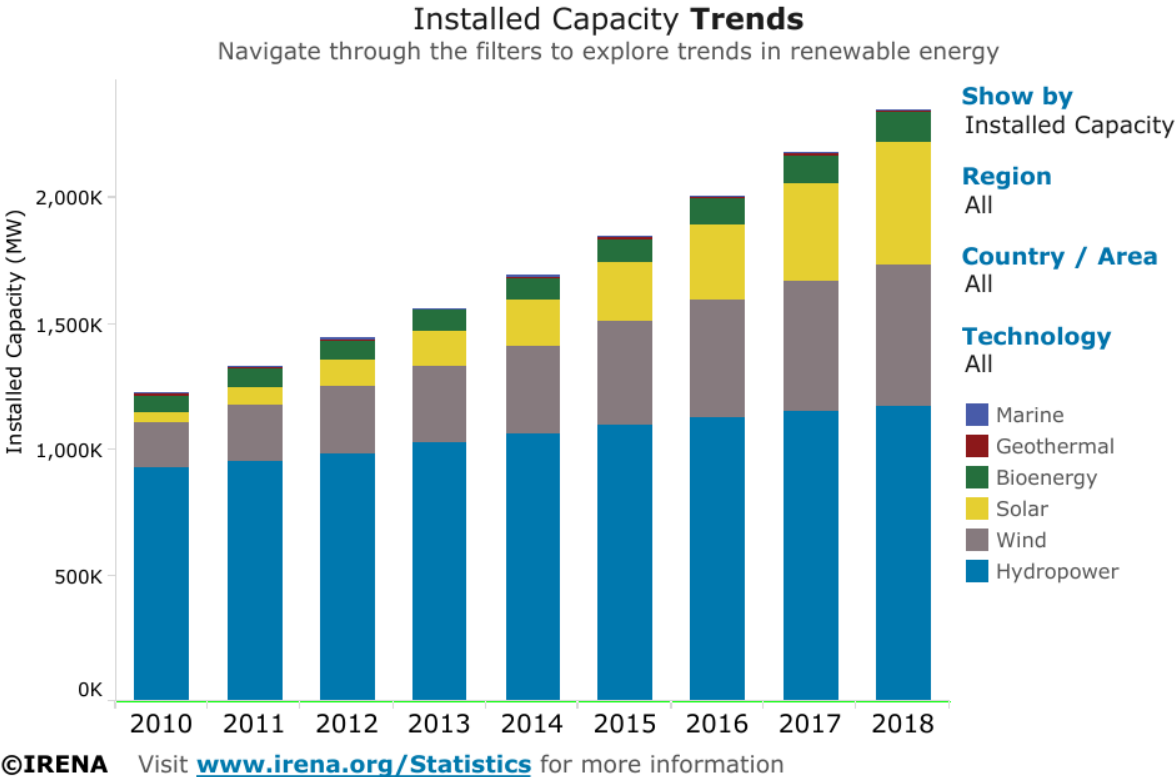
Figure 1 Installed capacity trends from 2010 to 2018 for renewable energy[1]

From figure 2, the global battery energy storage market volume is 4978MW at 2018 which is 7 times larger than the size in 2013, at it expected to be 22207MW in 2023. This enormous potential market has motivated researchers to find a cost-effective and environmentally friendly BESS. Figure 3 shows a steady increase in the batteries market over the past years. It also shows the battery energy storage system with dominant battery market share, which includes lithium-ion (LIB), nickel-metal hydride (NiMH) and nickel-cadmium (NiCD) and lead-acid batteries. From 2000 to 2017, the demand for lead-acid batteries only increased by 30%, and the increasing speed further decreased in recent years. The demand for lithium ion batteries increased fast from 2005 to 2015, but the dramatically increased cost of lithium material limited its application in BESS. Moreover, all of these commercial battery systems have some ecological, economic, and safety problems.
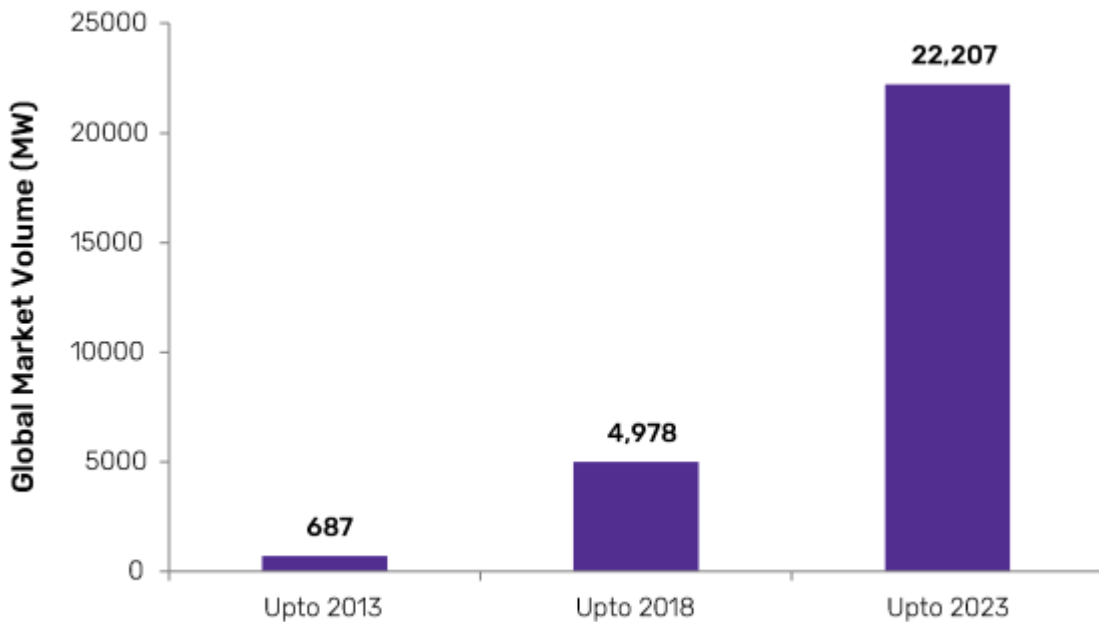
Figure 2 Global Battery Energy Storage Market Capacity (MW) 2013-2023[3]
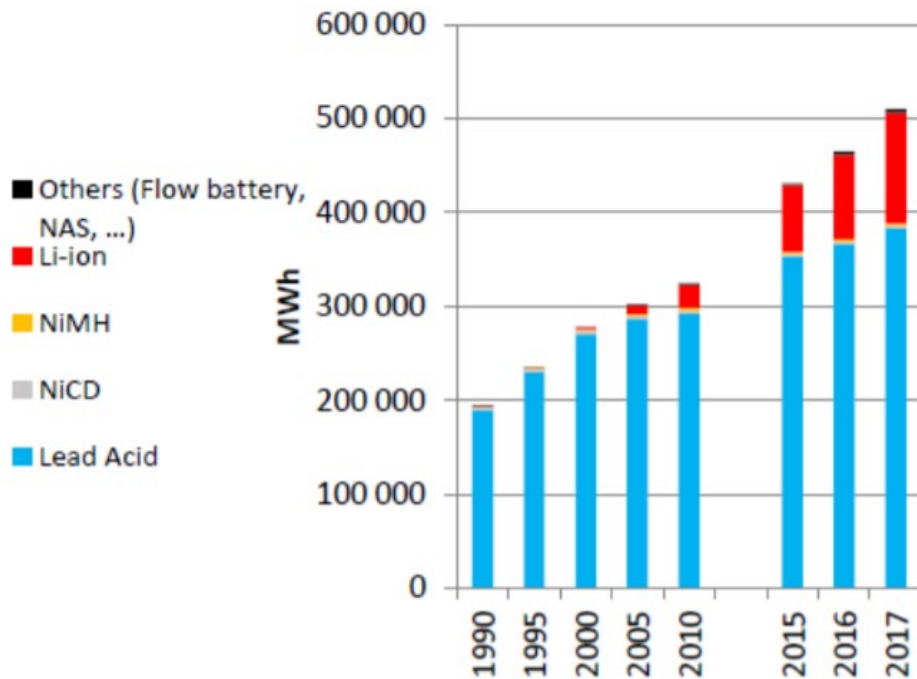
Figure 3 Demand for major battery systems over the past years[4]

Firstly, lead-acid and nickel-cadmium batteries all use toxic metal as electrode which makes their disposal an environmental concern, in addition to the energy density of lead-acid and nickel-cadmium batteries are only 30 Wh kg^{-1}.[5, 6] Nickel-metal hydride battery has a high energy density, but it is expensive, limited high rate capacity and low coulombic efficiency.[7-9] The electrolyte of commercial lithium ion batteries is $LiPF_6$ dissolved in carbonate ester which is flammable and toxic.[10] Furthermore, $LiPF_6$ is sensitive to air, so the whole assembly process should be operated in an oxygen-free environment which means high prime cost.[11]

1.2 Aqueous rechargeable batteries

In contrast, aqueous rechargeable batteries (ARBs) can be a promising candidate for the next generation of BESS for some reason. The inherent advance for ARBs is aqueous electrolyte, which has a two-order magnitude higher of ionic conductivity than the organic electrolyte in LIB.[12] Hence, ARBs have high fast charge/discharge efficiency and rate capacity. Moreover, the electrolyte salt and solvent are much cheaper, and the cost of battery assembling is highly reduced than others. Furthermore, the normal electrolyte salt used in ARBs is non-toxic and environmentally friendly and easy for recycling.[13]

The first prototype of the aqueous rechargeable battery was reported by Dahn in 1994 which uses $LiMn_2O_4$ (LMO) and β-VO_2 as cathode and anode, respectively.[14] Figure 4 illustrate the working mechanism of the battery during the charge/discharge process. The lithium ion inserts in or extracts from the active material during the cycling, and the reactions are given as [1]and [2][14]:

$$LiMn_2O_4 \rightleftarrows Li_{1-x}Mn_2O_4 + xLi^+ + xe^- \quad [1]$$

$$VO_2(\beta) + xLi^+ + xe^- \rightleftarrows Li_xVO_2 \quad [2]$$
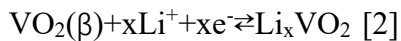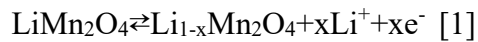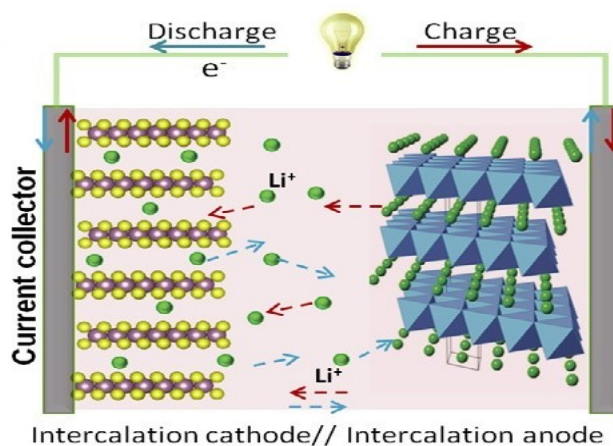
Figure 4 Working mechanism of the LMO/β-VO2 battery[15]

After that, significant progress was made in this area by exploring more new types of ARBs, and more fundamental battery chemistries. Table 1 contains the recent progress of various ARBs. As the table shows, ARBs can be generally classified by four types include aqueous rechargeable lithium ion batteries (ARLBs), aqueous rechargeable sodium ion batteries (ARSBs), aqueous rechargeable zinc ion batteries (ARZBs), and aqueous rechargeable hybrid batteries (ARHBs).

Table 1 Recent progress of various ARBs.[15]

Cell type	Electrolyte	Working voltage(V)	Capacity retention (%)	Initial capacity (mAh g^{-1})
Aqueous rechargeable lithium ion batteries (ARLBs)				
$LiMn_2O_4$ nanochains//AC	0.5 M Li2SO4	0-1.8	~100% (200) at 4.5 C	110
Porous $LiMn_2O_4$//AC	0.5 M Li2SO4	0-1.8	93% (10000) at 9 C	~115
$LiMn_2O_4$ nanochains//PPy@MoO_3	0.5 M Li2SO4	0-1.95	~90% (150) at 4.5 C	~88
$LiFePO_4$@C//LiV_3O_8	9 M LiNO3	0-0.8	~91.8% (100) at 10 C	90

LiFePO$_4$//LiTi$_2$(PO$_4$)$_3$	0.5 M Li$_2$SO$_4$+0.1 M LiOH, absence O$_2$	0-1.4	90% (1000) at 6 C	N/A
Aqueous rechargeable sodium ion batteries (ARSBs)				
Na$_{0.44}$MnO$_2$//NaTi$_2$(PO$_4$)$_3$	1.0 M Na$_2$SO$_4$	0.1-1.4	> 1000 cycles at 7 C	~127 Wh L^{-1}
Na$_2$FeP$_2$O$_7$//NaTi$_2$(PO$_4$)$_3$	1.0 M Na$_2$SO$_4$ or 4.0 M NaClO$_4$	0-1.4	2.0 mA cm^{-1}	~45
Na$_3$MnTi(PO$_4$)$_3$// Na$_3$MnTi(PO$_4$)$_3$	1.0 M Na$_2$SO$_4$	0.4-1.8	98% (100) at 1 C	~56.5
Na$_3$V$_2$(PO$_4$)$_3$//NaTi$_2$(PO$_4$)$_3$	1.0 M Na$_2$SO$_4$	0.5-1.6	50% (50) at 10 A g^{-1}	~58
Na$_2$CuFe(CN)$_6$//NaTi$_2$(PO$_4$)$_3$	1.0 M Na$_2$SO$_4$	0.2-1.8	88% (1000) at 10 C	85
Aqueous rechargeable zinc ion batteries (ARZBs)				
β-MnO2//Zn	3.0 M Zn(CF$_3$SO$_3$)$_2$+0.1 M Mn(CF$_3$SO$_3$)$_2$	0.8-1.9	94% (2000) at 6.5 C	150
ZnMn$_2$O$_4$@C//Zn	3.0 M Zn(CF$_3$SO$_3$)$_2$	0.8-1.9	94% (500) at 500 mA g^{-1}	85
Zn$_{0.25}$V$_2$O$_5$·nH2O//Zn	1.0 M ZnSO$_4$	0.5-1.4	80% (1000) at 8 C	260
α-MnO2//Zn	1.0 M ZnSO$_4$	1.0-1.9	~100% (100) at 6 C	~100
Aqueous rechargeable hybrid batteries (ARHBs)				
LiMn$_2$O$_4$//Zn	3 M LiCl+4 M ZnCl$_2$+0.1 M KOH	1.4-2.1	90% (1000) at 4 C	115
LiFePO$_4$//Zn	1M CH$_3$COOLi+ 1M Zn(CH$_3$COO)$_2$	0.5-1.7	> 95% (125) at 1 C	100
Na$_{0.44}$MnO$_2$//Zn	1 M Na$_2$SO$_4$+0.5 M ZnSO$_4$	0.5-2	Above 90% (100) at 4 C	40
NiHCF//Zn	0.5 M Na$_2$SO$_4$+0.05 M ZnSO$_4$	0.9-1.9	81% (1000) at 500 mA g^{-1}	76.2

1.2.1 Aqueous rechargeable zinc ion battery based on cation-deficient spinal ZnMn2O4 cathode and zinc foil as the anode

The cation-deficient spinal $ZnMn_2O_4$ (ZMO) based ARZB was proposed by Chen's group in 2016 inspired by the widely used spinel $LiMn_2O_4$ cathode in LIBs. Figure 5 shows the proposed Zn^{2+} diffusion pathway in ZMO spinel with and without Mn vacancies. For a perfect ZMO spinel structure, when the zinc ion transport from one 4a site to another passing through 8c site, it will endure a huge electrostatic repulsion from the manganese ion in a neighboring octahedral site (8d). On the contrast, the ZMO spinel structure is filled with manganese vacancies allows easier zinc ion diffusion, leading to high zinc mobility and initial capacity.[16]
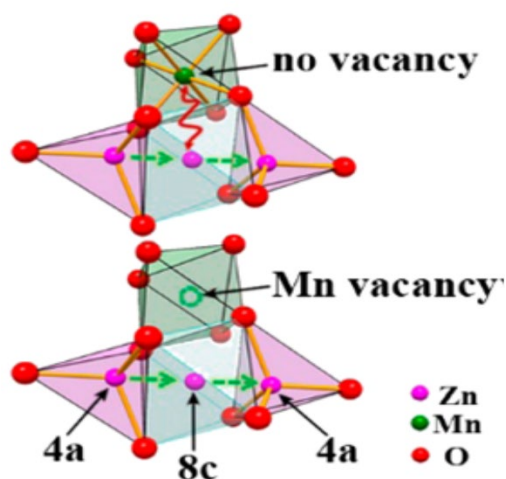
Figure 5 Schematic illustration of Zn^{2+} diffusion pathway in ZMO spinel without and with Mn vacancies[16]

The cathode material was synthesized through facile solution-based oxidation–precipitation and crystallization process at modest condition mixed with carbon, so-called coupled spinel ZMO/carbon nanocomposite[17]. Figure 6 illustrates the process of synthesis ZMO/C nanocomposite. Zinc nitrite and manganese nitrite were oxidized and the products precipitated. Then the precipitant was washed, centrifuged and dried.
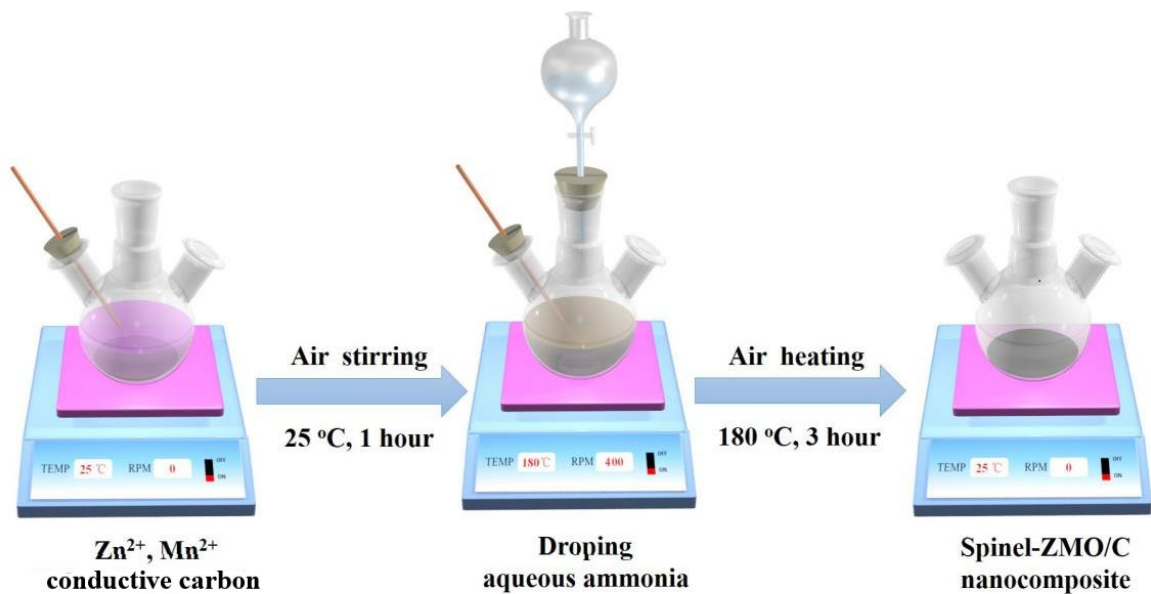
Figure 6 Schematic illustration of the synthesis of spinel ZMO/C nanocomposite[16]

Figure 7 shows the working principle of ZMO/Zn battery during the charge and discharge process. When the battery is charging, the zinc ions extract from the spinel ZMO cathode. Meanwhile, the zinc ions in the electrolyte will gain 2 electrons and deposit on the zinc foil. In contrast, zinc from anode lost two electrons and dissolved into the electrolyte, but the zinc ions insert into the cathode material during the discharge process. The working potential window is 0.8-1.9V. The reactions of the electrodes during the charge and discharge process can be written as:

$$ZnMn_2O_4 \rightleftarrows Zn_{1-x}Mn_2O_4 + xZn^{2+} + 2xe^- \text{ [3]}$$

$$Zn^{2+} + 2e^- \rightleftarrows Zn \text{ [4]}$$
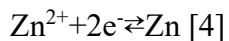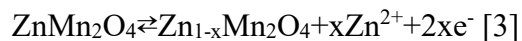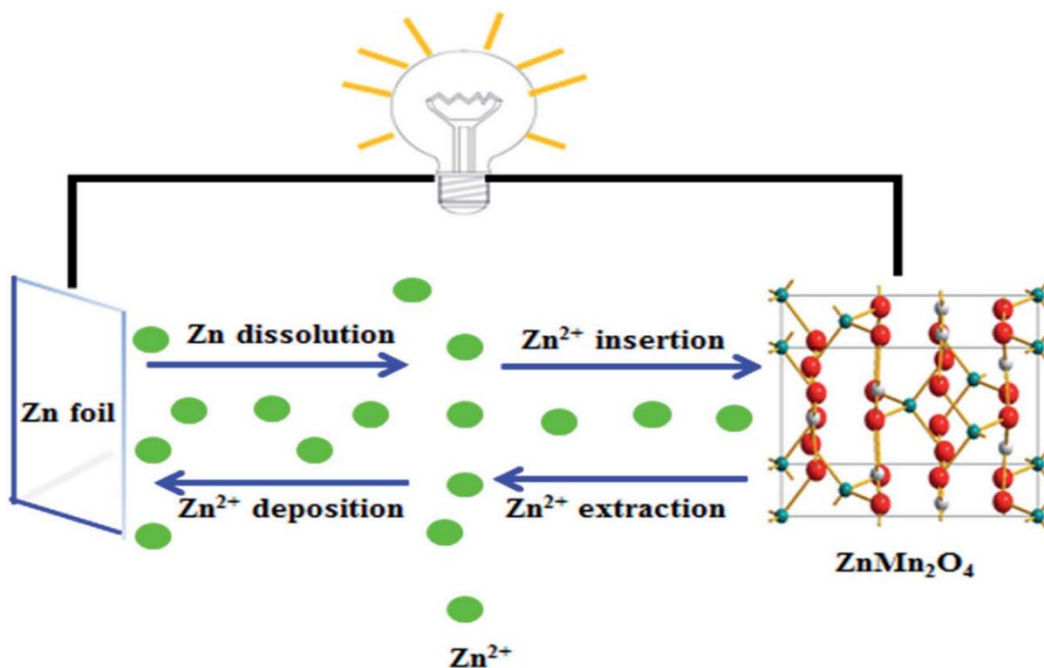
Figure 7 Schematic illustration of the charge/discharge process of ZnMn$_2$O$_4$/Zn.[21]

The electrolyte for ZMO/Zn battery is zinc trifluoromethanesulfonate (Zn(CF$_3$SO$_3$)$_2$) which is a bulky-anion zinc salt and has been widely applied in solid electrolyte or gel electrolyte for its high ionic conductivity.[18] Figure 8 shows the Cyclic voltammograms of the Zn electrode in the aqueous electrolyte with varied Zn(CF$_3$SO$_3$)$_2$ concentration. The corresponding onset potentials of initial Zn plating/stripping are −0.14/−0.050 V and −0.17/−0.055 V, respectively. The smaller potential separation between plating and stripping and higher response current can be found for Zn(CF$_3$SO$_3$)$_2$, suggesting good reversibility and fast kinetics of Zn deposition/dissolution.[17]
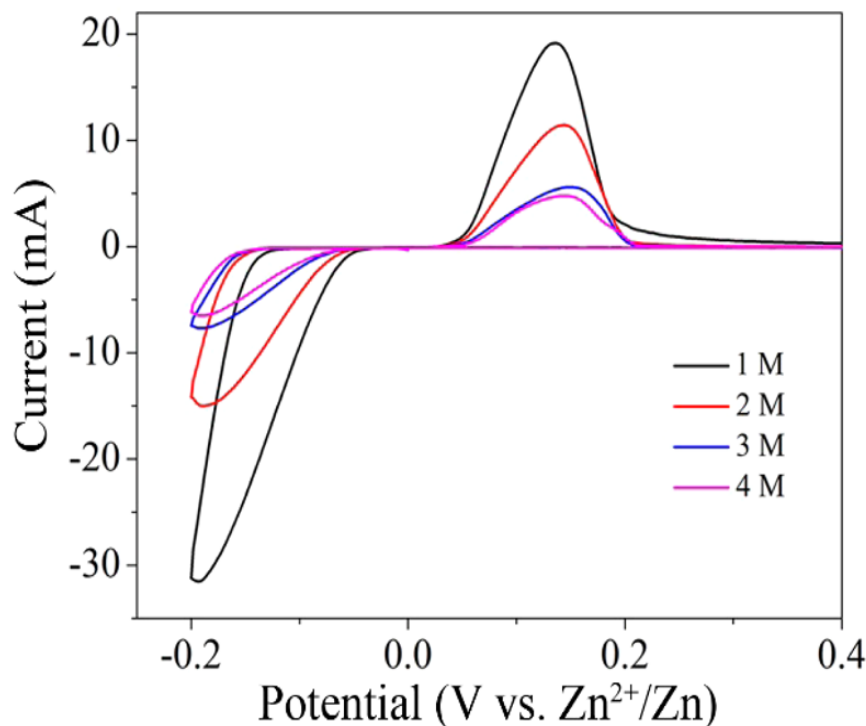
Figure 8 Cyclic voltammograms of Zn electrode in aqueous electrolyte with varied Zn(CF₃SO₃)₂ concentration[17]

1.2.2 Limitations of ZMO cathode based aqueous rechargeable zinc ion batteries

The stability of the active material is a persisted problem for all manganese-based cathode which includes $LiMn_2O_4$, MnO_2, $ZnMn_2O_4$.[19-21] Those manganese-based cathodes all have Mn^{3+} in the structure. During the charge and discharge process, the Mn^{3+} will tend to have an irreversible disproportionation reaction ($2Mn^{3+} \rightarrow Mn^{2+} + Mn^{4+}$) and dissolved from the electrode into the electrolyte.[22] The dissolution rate speeds up at high temperature and low PH.[27] This progress will destroy the structure of the cathode, and cause capacity fading. Moreover, the capacity of ZMO based ARZB highly depends on the manganese vacancies. The theoretical capacity for ZMO cathode is 224mAh·g⁻¹, but the actual largest initial capacity for ZMO is about 150mAh·g⁻¹ due to the structure stability and electrostatic repulsion.[17, 21] Another problem is

10

about the zinc anode, which is wildly applied in ARZBs. By the instinct property of zinc cation, the PH value of zinc salt electrolyte is always around 4 or less. The mild acidic electrolyte will corrosive the zinc anode and also leads to the dendrite formation along the anode surface.[23,24] For cost-effective consideration, the electrolyte salt for ZMO battery is another problem. $Zn(CF_3SO_3)_2$, a costly zinc salt, which is almost 25 times higher compared with the zinc sulfate based on the quote from Sigma-Aldrich.

1.2.3 Strategies to overcome the manganese dissolution

Manganese disproportionation reaction and dissolution has been a critical problem for the commercialization of manganese-based cathode material include MnO_2, $LiMn_2O_4$ and $ZnMn_2O_4$. Kinds of strategies have been reported to inhibit the manganese dissolution includes adding additives into the electrolyte, and surface coating.[21, 25]

Wu et al. reported that adding manganese ions into the electrolyte can effectively migrate the manganese dissolution and improve the capacity for ZMO based battery.[21] The electrolyte in that work is 1M zinc sulfate mixed with 0.05M manganese sulfate. By the characterization, the zinc diffusion rate was increased after adding manganese sulfate into the electrolyte. The manganese dissolution is also partially inhibited by equilibrium of the manganese disproportionation reaction.[26]

Walz et al. demonstrated that the surface coating of nanoporous ZrO_2 and TiO_2 on the $LiMn_2O_4$ cathode has the significant effect of improving the structural stability even at high temperature.[25] The nanoporous ZrO_2 and TiO_2 coated cathode were synthesized by sol-gel method at a 4wt%. The average size of the nano ZrO_2 and TiO_2 particles are about 3.3nm and

4.8nm, respectively. The batteries with the oxides coating show the excellent stability at high temperature compared with the uncoated ones.

1.2.4 Strategies to inhibit the dendrite formation

Dendrite formation has been an inherent and serious problem for all the metal anode include lithium metal anode and zinc metal anode. Zinc metal anode is widely used in ARZBs, and zinc deposition/dissolution is a significant process during cycling.[28] However, the ununiform electrodeposition caused the zinc dendrite. The dendrite is continually growing along with the cycling, finally, pierce the separator and cause the short circuit. There is plenty of researches about migrating the zinc dendrite formation. The methods mentioned here include adding additives into electrolyte, surface coating and optimization of electrolytes.[29-31]

Mitha et al. reported that adding polyethylene glycol into aqueous electrolyte as additive can suppress the zinc dendrite formation significantly. The polyethylene glycol with the molecular weight of 200 was added into the 2M $ZnSO_4$ and 1M Li_2SO_4 electrolyte with the amount of 1vol.% and stirred for 6 hours. The capacity of the batteries with PEG added electrolyte was increased significantly. Moreover, the dendrite formation was suppressed effectively by the absorption of PEG on the anode surface, which helped the zinc deposit more uniformly.[29]

Ahmed et al. fabricated artificial solid electrolyte interface onto the anode surface by ultrathin graphene films to migrate the zinc dendrite. The porous zinc anode was coated by graphene oxide first, and the graphene oxide was reduced by water vapor to form graphene based artificial solid electrolyte (G-SEI). The characterization results reveal that the G-SEI has the

ability to control the ion transport between the electrolyte and the anode surface, and also promotes a uniform deposition (less dendritic growth) of zinc on the anode.[30]

Tuan et al. reveal the effect of gel electrolyte on inhibiting the zinc dendrite formation in aqueous rechargeable batteries system. The aqueous electrolyte was mix with 5wt% of fume silica to form the gel electrolyte.[31] The previous studies have proved that the increased viscosity of electrolyte, the lower cation/anion transportation, but higher stability of both cathode and anode.[32] Moreover, Tuan et al. also added lead cations into the electrolyte to further suppress the dendrite growth. Lead ions can be reduced prior to zinc, and can serve as the substrate for zinc deposition. This more positive substrate can lead to the even deposition of zinc, and suppress zinc dendrite by regulating the current distribution.[33]

1.3 Gelatin

Gelatin is a polypeptide and normally obtained by partial hydrolysis of collagen. Figure 9 shows the structure of collagen and gelatin. Collagen is a sufficient protein in animals. Collagen consists of polypeptides wound together to form triple-helices of elongated fibrils which have strong mechanic properties, and is the main component of connective tissue. Gelatin is normally fabricated by the partial hydrolysis of collagen to destroy the triple-helices structure in hot water

or dilute acid. Gelatin contains kinds of amino acid such as glycine, proline, hydroxyproline, etc. Figure 10 shows the exact composition percentage of gelatin.
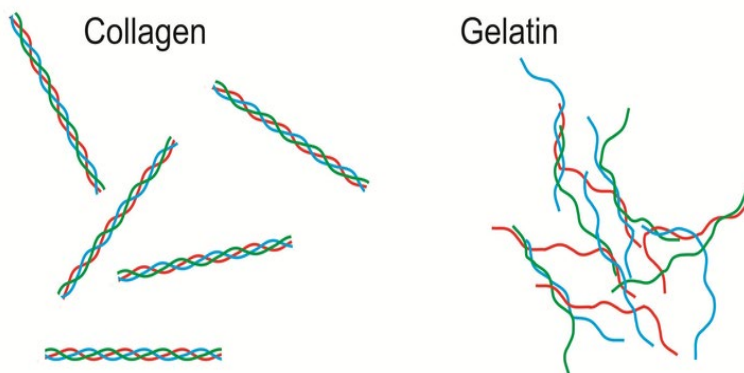
Figure 10 The structure of collagen and gelatin[34]

Figure 9 Amino acid composition of

1.3.1 Gelatin in Industrial Electrodeposition

Gelatin is commonly performed as a gelling agent in the food industry, drug capsules, and maquillage. However, gelatin was firstly reported by A.G. Betts as additives used in industrial metal electrodeposition in 1903.[36] Since then, gelatin has been widely used in metal electrodeposition includes copper, zinc, tin, and bismuth in the acidic aqueous electrolyte.[37, 39, 40, 41] In 2014, Meudre and Ricq reported the gelatin additive in the electrolyte have the ability to inhibit the initial nucleation of the deposited metal and promote homogenous and small crystallites.[37] Figure 11 is the SEM images of copper deposit obtained for 30 min with and without gelatin additives. The smooth plating is attributed to the absorption of gelatin during the electrodeposition.[37] The majority of amino acid in gelatin is glycine, and from previous reports, Cu^{2+} cation can be chelated by glycine to form $CuGl^+$, $CuGl_2$, and $CuGl_3^-$ based on the electrolyte PH.[38] In Meudre's work, the PH value of electrodeposition bath is 1, which means only $CuGl^+$ can be formed. Then the positively charged gelatin and copper complexes will be absorbed on the working electrode by the applied voltage. The gelatin adsorption film can be characterized

14

and confirmed by quartz crystal microbalance, Fourier transform infrared spectroscopy (FTIR), and Atomic force microscopy (AFM). The gelatin film can cover the active sites on the working
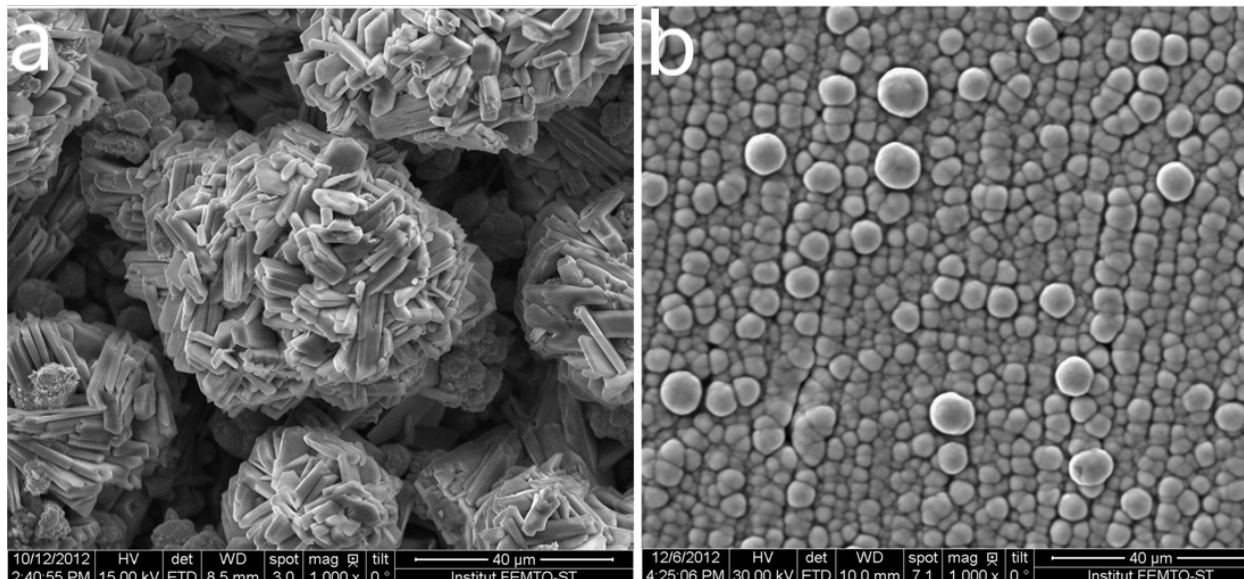
Figure 11 SEM micrographs of copper deposit obtained for 30 min from an electrolyte contains (a) no additives; (b) 1g/L gelatin[37]

electrode, and decrease the nucleation rate, which finally, in turn, get a smooth coating. [37, 39]

1.3.2 Gelatin as Solid Electrolyte

Because of the high ionic conductivity of gelatin, gelatin has also been used as a solid electrolyte in the electrochromic device (ECD) or solid-state battery systems. Table 2 shows the ionic conductivities of several common polymer matrices based on zinc salt. C. Zhi reported a novel hierarchical polymer solid electrolyte (HPE) based on gelatin and PAM. By the contribution of HPE, an extremely safe and wearable solid-state zinc ion battery was investigated.[42]

Table 2 Comparison of gelatin with some zinc-salt-polymer-electrolytes in terms of ionic conductivity in the literatures[42]

Polymer matrices	Ionic conductivity (mS cm^{-1})	Zinc salts

Gelatin	5.68	$ZnSO_4$
PEO	2~4	$ZnCl_2$
Poly-ε-caprolactone	0.88	$Zn(CF_3SO_3)_2$
Poly(4-vinylpyridine)	$2\times10{-}5$	$Zn(ClO_4)_2$
PAN	0.22	$ZnSO_4$

Figure 12 illustrates the schematic of the synthesis route to the HPE. Briefly speaking, gelatin, potassium persulfate, Acryl amide (AM) monomers and N,N'-methylenebisacrylamide (BIS) was mixed and added into the mixture solution of zinc sulfate and manganese sulfate. Then, the mixture solution was injected into the porous electrospun PAN membrane and dried for 2-3 hours.[42]

The cathode material of the zinc ion battery is α-MnO_2, and zinc is the anode. Solid electrolyte can be a strong physical barrier to inhibit the dendrite growth. Moreover, manganese cannot be dissolved in the solid electrolyte, which significantly enhanced the stability of the

cathode material. As a result, the battery shows excellent stability, which has 97% capacity retention after 1000 cycles.[42] Hence, gelatin has great potential in the battery system.
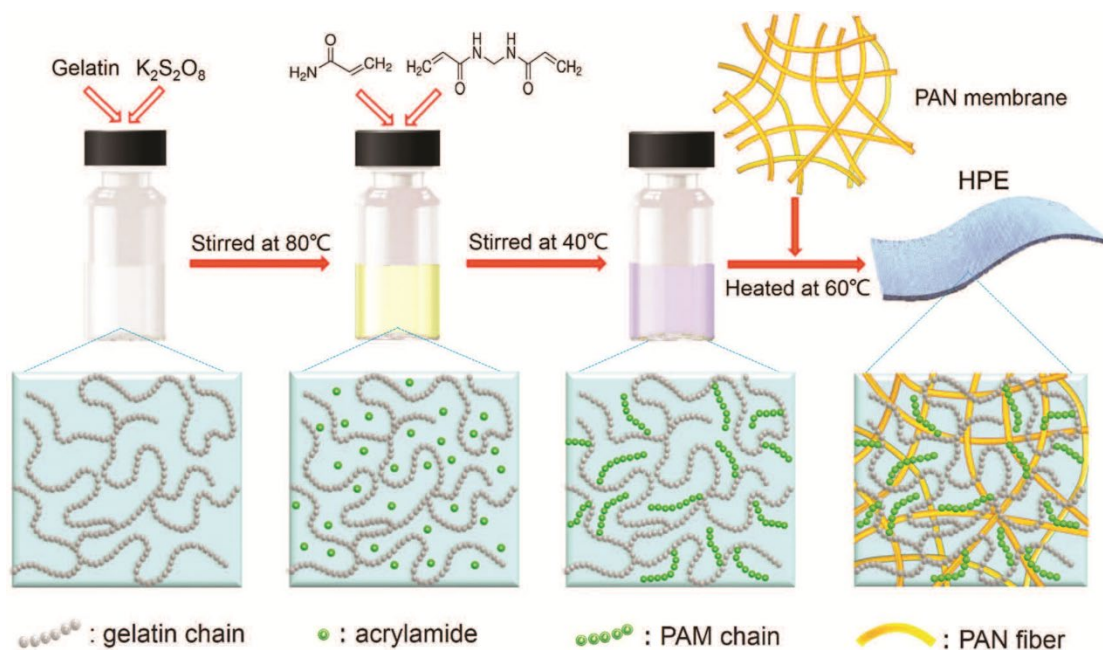
Figure 12 Schematic of the synthesis route to the HPE[42]

1.4 Project scope and objectives

Overall, this work mainly focuses on two parts.

1. <u>Synthesize zinc manganese oxide with more manganese vacancies to promote higher initial capacity with zinc sulfate as electrolyte.</u> The theoretical capacity of ZMO is $224mAh \cdot g^{-1}$, but the capacity of original ZMO is only 150 $mAh \cdot g^{-1}$ at low current density.[16,21] In this work, the synthesizing method is slightly changed in order to get manganese vacancies abundant ZMO.

2. <u>Introduce the gelatin to this aqueous rechargeable zinc ion battery to stabilize the system.</u> The electrolyte used in this work is mildly acidic, which means favorable for dendrite growth. Moreover, defect abundant structure also indicates poor stability, so gelatin is applied in this work to inhibit dendrite growth, and also stabilize cathode structure.

Chapter 2: Characterization Techniques

2.1 Material Characterization Techniques

2.1.1Scanning Electron Microscope (SEM)

Scanning electron microscope (SEM) is a common characterization technique to obtain the surface topography and composition information of samples at the nanoscale. It has typically several modes that can be operated, which are secondary electron (SE) image, backscattered electron (BSE) image, and energy dispersive x-ray (EDX). Secondary Electrons generated on the surface of a specimen by the energy gained from inelastic collision with beam electrons. The secondary electrons have lower kinetic energy, and have less interaction volume compared with backscattered electrons. So, secondary electron form images are normally used to show the topography of the sample. Backscattered electrons consist of high-energy electrons originating in the electron beam, which are reflected or back-scattered out of the specimen interaction volume by elastic scattering interactions with specimen atoms. Since heavy elements (high atomic number) backscatter electrons more strongly than light elements (low atomic number), and thus appear brighter in the image, BSEs are used to detect contrast between areas with different chemical compositions. X-ray is generated when the sample is bombarded by high energy electrons and knock off the core electrons of the sample and is left with a vacant energy level. Then the outer-shell electron will fall into the vacant energy level and emit photons with quantized energy which is the x-ray. Because each element has a unique set of energy levels, the x-ray signal can be detected by the energy dispersive x-ray detector to map the distribution or the abundance of elements in the sample.

Figure 13 is the schematic of the fundamental internal component of SEM. Voltage is applied on the electron gun to release electrons, and the electrons are accelerated by the anode. The magnification can be adjusted by the electromagnetic lens and coils. Then the electron beam is injected to the specimen with raster scan pattern. For each scan point, the signal includes SE, BSE and x-ray were detected and converted to image on the computer.
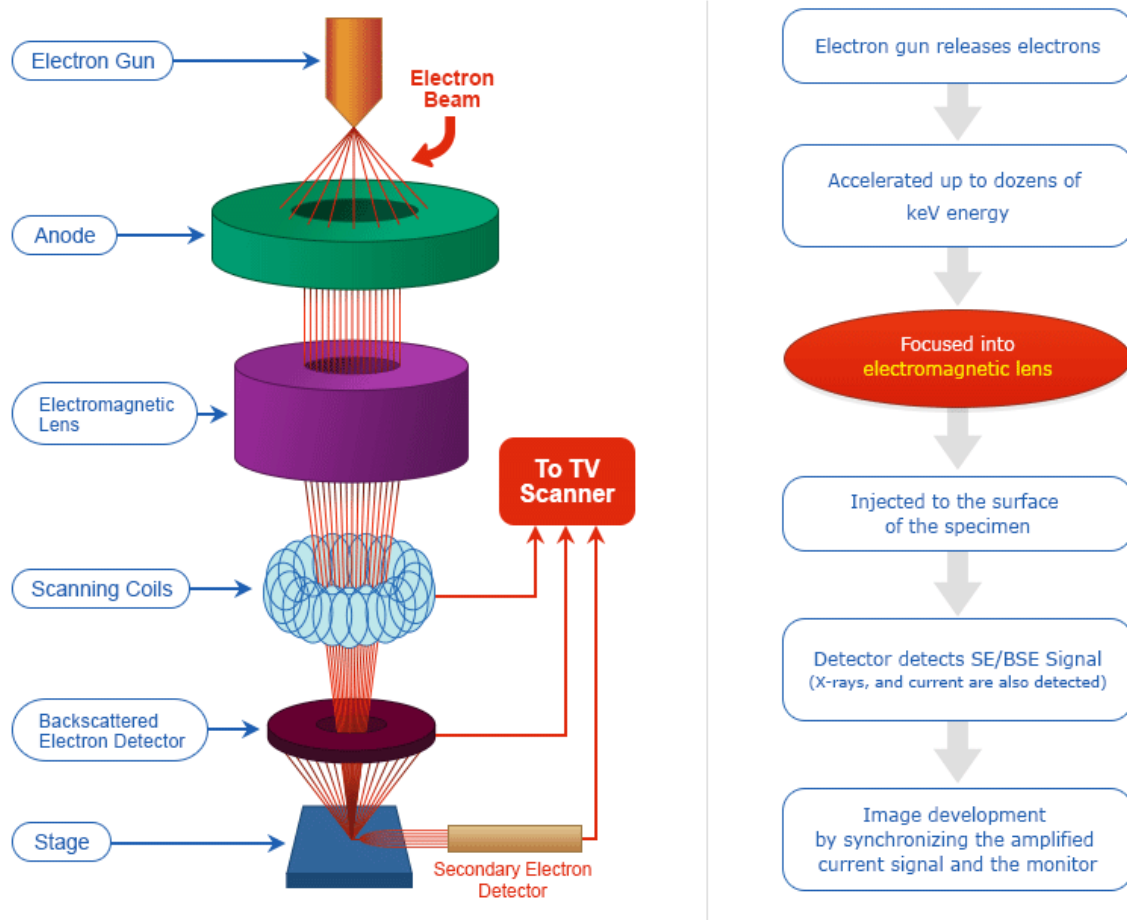
Figure 13 Schematic of Scanning Electron Microscope[43]

In this work, SEM for all samples was performed on UltraPlus FESEMs (Zeiss) with an accelerating voltage of 10kV.

2.1.2 X-ray Diffraction (XRD)

X-ray Diffraction is an analytical technique widely used to identify the crystal structure and crystallinity. X-ray diffractometers mainly consist of the X-ray source, sample holder and counting detector. As figure 14 shows, x-ray is generated by X-ray source and passes through the collimator. Then, the incident x-ray strikes the sample surface, the x-ray can be reflected, scattered, or absorbed by the sample, and the x-ray signal is collected by the detector and identify the intensity. X-ray source and detector will rotate along the testing process, and data will be recorded at every rotate. The final result will be a diagram of signal intensity at each incident angle.
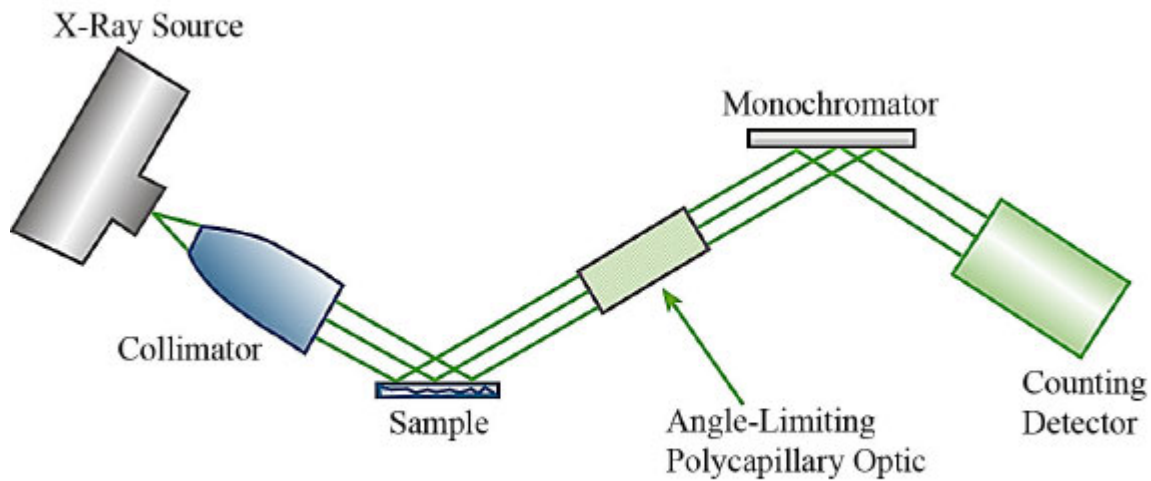
Figure 14 Schematic of X-ray diffractometer[44]

The relation between the incident angle and signal intensity is based on Bragg's Law, which is

$$n\lambda = 2d\sin\theta \ [5]$$

Where n is an integer number, d is the spacing between two planes, λ is the wavelength of the generated x-ray, and θ is the incidence angle. Furthermore, once the distance between crystal

planes is known, the Miller index of that particular crystal plane (for cubic structures) can be determined using the equation:

$$d = \frac{a}{\sqrt{h^2+k^2+l^2}} \quad [6]$$

Where a is the unit cell length and h, k, and l are the Miller indices associated with that particular crystal plane. Figure 15 shows how the x-ray interact with a typical crystalline sample. Moreover, the XRD spectrum can also tell the average size of the crystal by the Scherrer method:

$$d = \frac{K\lambda}{(FWHM)\cos\theta} \quad [7]$$

Where d is the size of the crystal, K is the Scherrer shape constant, λ is the wavelength of the X-rays, FWHM is the full width at half maximum of the corresponding peak in the XRD spectrum, and θ is the incidence angle. Some common K values from literature are 0.94 for spherical crystals, 1.00 for nanorods, and 0.89 for platelets.[45]

In this work, XRD characterization was carried out on a Bruker D8 Discover X-ray diffractometer using a copper target and a wavelength of 0.154 nm (Cu Kα). The measurement range was 5°-90° at a scan rate of 0.2 degrees per second.

2.1.3 Fourier Transform Infra-red Spectroscopy (FTIR)

FTIR spectroscopy is used to get the spectrum of absorbance of infra-red light for different materials. As infra-red light passes through a molecule, certain wavelengths will be absorbed and be converted to the physical motion of the covalent bond. With exposure to infra-red radiation, molecules experience a change in their dipole moments leading to a change in the energy state. This excitation can be manifest in stretching, twisting, scissoring, bending or

translation of a molecule. The transmitted light can be captured by a detector and analyzed to determine the types of bonds present in the sample.

Figure 15 shows the working principle of an FTIR interferometer. Normally, infra-red light is generated by firing a broad-band beam, and passes through a partially reflective mirror leading to beam splitting. The split beams are respectively directed to one fully reflective stationary mirror, and a fully reflective moving mirror. The split beams reflect off these mirrors, interact with the sample and are then collected at the detector. The moving mirror is used to add phase difference to the incident rays. During constructive interference (no path difference between infra-red rays from the moving and stationary mirrors) maximum signal reaches the detector after passing through the sample. In contrast, when the interference is destructive, no signal is expected at the detector. The measurement is carried out at a variety of phase angles producing an interferogram at the detector. This is then converted to a frequency spectrum using a Fourier transform. The spectrum can be compared to databases to identify specific bonds responsible for the absorption of light, and through this, the entire molecular landscape can be identified.
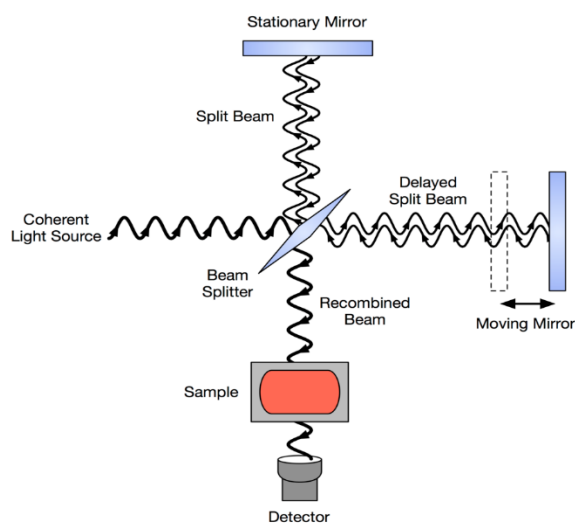
Figure 15 Schematic of an FTIR interferometer[46]

FTIR spectroscopy in this work was performed on a Bruker Optics Vertex 70 Spectrometer in the wavenumber range of 400 cm-1 to 4000 cm-1 with a repetition of 20 scans.

2.1.4 Thermogravimetric analysis (TGA)

Thermogravimetric analysis is a thermal analytical method to record the weight changes of samples over time with increasing temperature which normally used to evaluate the thermal stability of the sample. TGA can be operated in different atmospheres include ambient air, vacuum, oxidizing gases, and corrosive gases depend on the researchers. Figure 16 illustrates the working principle of TGA. The sample will be heated by the furnace at a constant rate, and the mass changes will be recorded by the balance and send to the computer. Moreover, the heat flow will also be tested by the thermocouple.
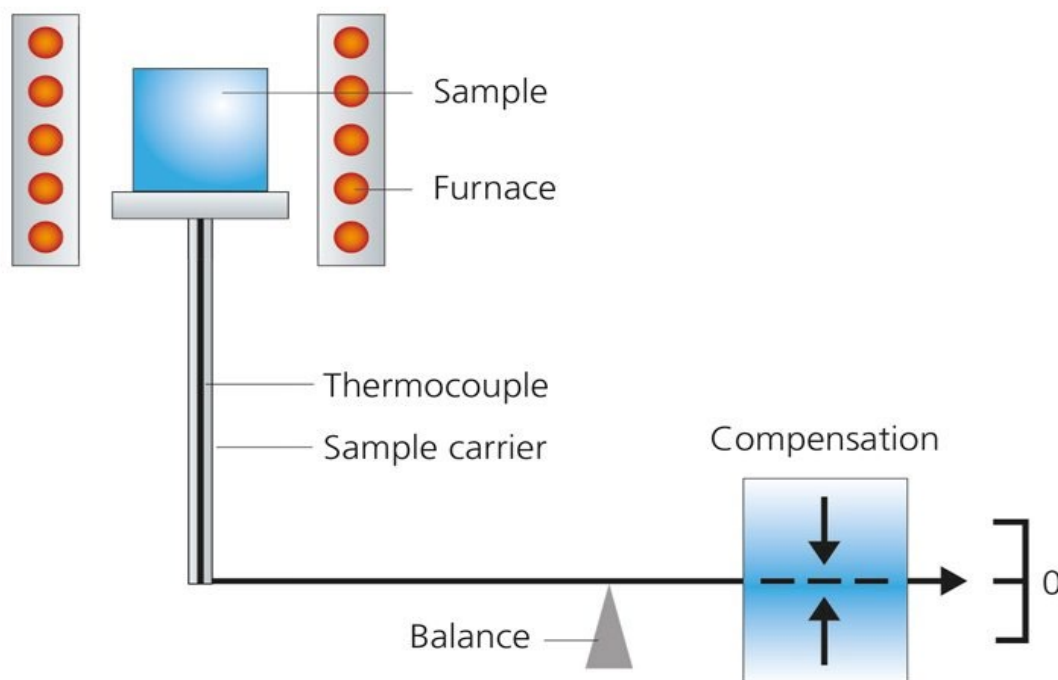
Figure 16 Working Principle of Thermogravimetric Analysis[47]

In this work, TGA was operated at a temperature range between 30℃ to 700℃ at a constant heat speed of 10℃/min.

2.1.5 X-Ray Photoelectron Spectroscopy (XPS)

X-ray photoelectron spectroscopy is a surface sensitive (7-11nm) characterization technique, which generally used for identifying the composition and chemical state of elements. As the figure 17(a) shows, the basic components of XPS include x-ray generator, sample holder, and photoelectron detector. The analysis is carried out in ultra-high vacuum. When the incident x-ray strikes electron of the surface atom, the electron gains energy. This energy can be sufficient for the electron to overcome the binding energy of the nucleus, and the remaining energy is converted to kinetic energy (Figure 17B). The velocity of these moving electrons is detected by the detector. The binding energy experienced by the electron is given by:

$$E_B = hv - E_k - \phi \ [8]$$

Where E_B is the binding energy of specific element, E_k is the kinetic energy of photoelectron detected, h is the Planck's constant, v is the frequency of the incident x-ray, and work function ϕ is an adjustable instrumental correction factor which normally is a constant and rarely needs to

be adjusted in practice. By the information of the binding energy, the composition and chemical

state of the sample can be easily identified.
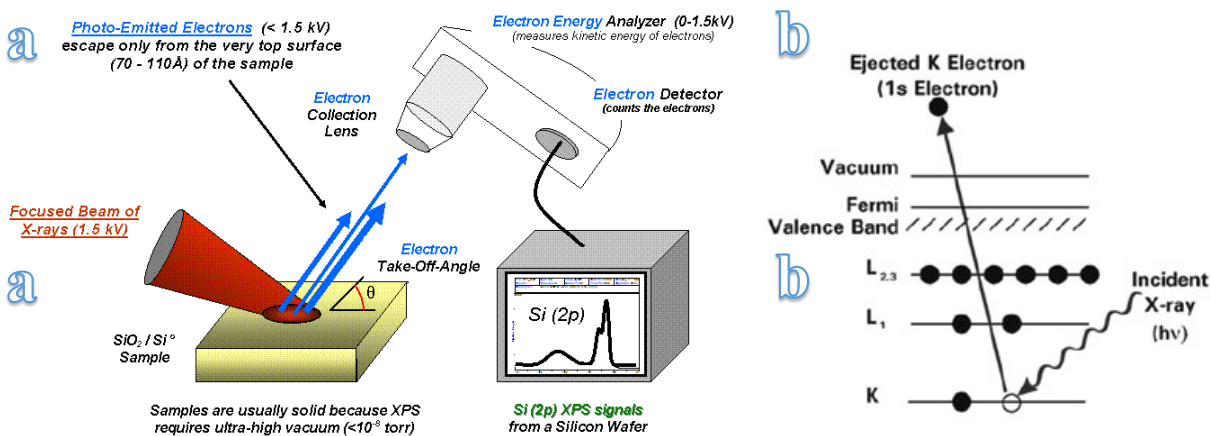
Figure 17 (a) Schematic of XPS instrument (b) principle of the emission of photoelectron[48,49]

  In this work, A Thermo-VG Scientific ESCALab 250 microprobe was used to record

XPS spectra. The spectra were taken at 1486.6 eV and 49.3 W, using a 200.0 μm beam size.

Reported binding energies were normalized against the C1s peak at 284.8 eV. The chamber

pressure was maintained at 2.0 nPa during testing. A wide survey (0-1350 eV) was conducted for

each sample to determine the surface elemental composition of the samples. This was followed

by scanning over a narrower energy window to obtain high energy resolution spectra of the

elements. The results were operated in CasaXPS vision 2.31, and the Shirley background type

was used for peak fitting.

2.2 Electrochemical characterization techniques

2.2.1 Chronoamperometry (CA)

Chronoamperometry is a time-dependent electrochemical technique that can be used to study electrodeposition behavior of ions on an electrode surface. There are two types of chronoamperometry that are commonly used, controlled-potential chronoamperometry and controlled-current chronoamperometry. For here, the controlled-potential chronoamperometry is introduced. As figure 18 shows, the constant potential between working electrode and counter electrode is maintained by potientostat. By the constant overpotential, the metal ions in the electrolyte will be reduced on working electrode, and the current change will be recorded and plotted as a function of time. Then, the processes of electrodeposition can be qualified by the plot.
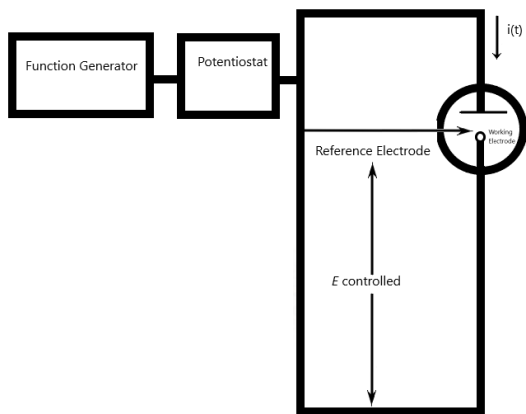
Figure 18 Scheme of Chronoamperometry Instrument[50]

Figure 19 describes these processes during reduction.[51] At the initial stage without overpotential applied, the system is at equilibrium and the oxidation and reduction reactions at the electrode are equal and thus there is no net transfer of electrons. After a potential is applied in Stage II, the electroreduction reaction begins. This represents the nucleation step. Once the nuclei are formed, the growth phase commences represented by Stage III. An understanding of the types and magnitudes of nucleation and growth reactions can be gained by analyzing chronoamperograms from different systems.
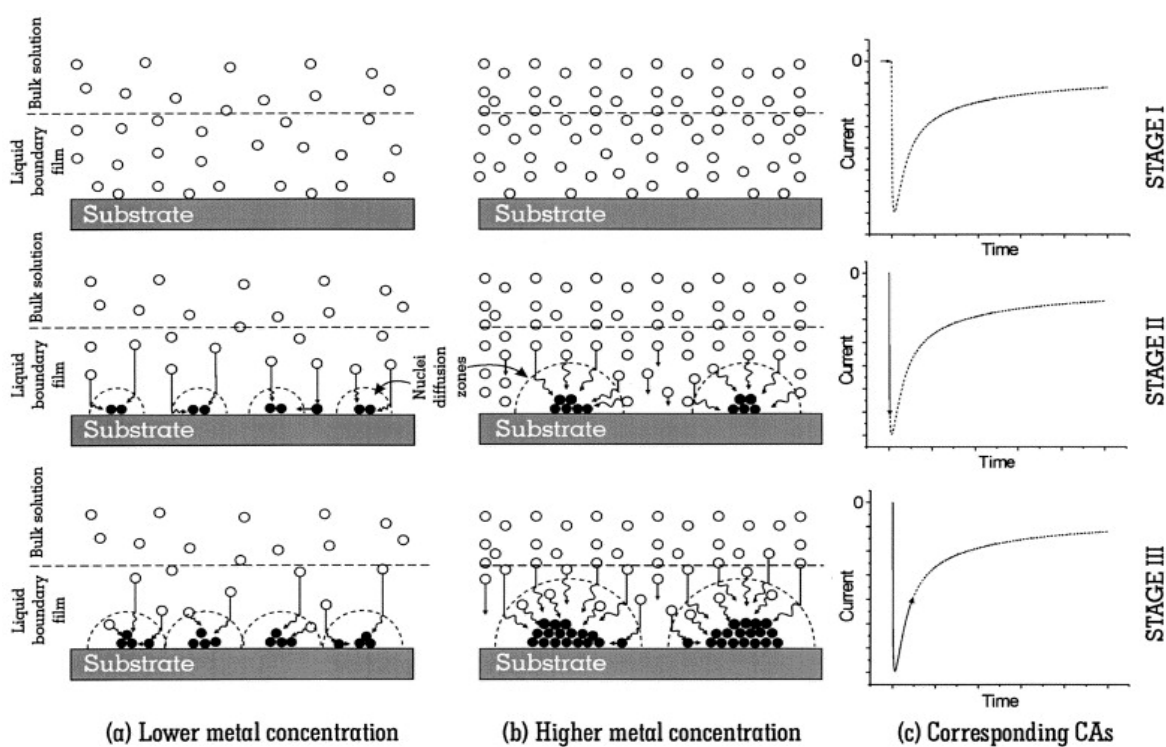
Figure 19 Schematic presentation of phenomena involved during copper nucleation at various stages of chronoamperometric experiment for (a) lower and (b) higher concentration of metal ions. Depicted stages are (I) prior to electroreduction, (II) state at the onset[51]

Chronoamperometry was measured using a Bio-Logic VMP3 electrochemical workstation. Zinc foil was used as both the working and counter electrodes, and Ag/AgCl were used as a reference electrode. Applied overpotential was set to -120 mV. Electrolyte is 2M zinc

sulfate with PH adjusted to 4. Chronoamperometry was conducted for different time durations depending on the investigation.

2.2.2 Cyclic Voltammetry (CV)

Cyclic voltammetry (CV) is an electrochemical technique used to study the oxidation and reduction potentials of molecular species. This technique is carried using two- or three-electrode system. In a typical cyclic voltammetry experiment, the working electrode is applied with a constant increasing rate versus time which called cathodic sweep. As the potential reaches the set voltage, the potential deceases at the same rate and back to the initial potential named as anodic sweep (Figure 20a). It also can be operated with constant decreasing potential first. The rate and repeat times can be adjusted as needed. A voltammogram is obtained by plot current versus potential.

Figure 20(b) is a typical cyclic voltammogram, where i_{pc} and i_{pa} show the peak cathodic and anodic current respectively for a reversible reaction. During this scan, the molecular species under investigation either gets reduced (or oxidized). At the initial voltage, the potential is too low for any reaction to happen and hence no current is measured. As the voltage is initially swept, reaction started to happen and current start to flow in the system. This current start to increase as the potential keeps on increasing. This current is due to the flow of ions from the bulk electrolyte to the electrode surface. At the electrode surface, the ions get reduced (or oxidized), and at these potentials, this reaction is limited by the diffusion of the ions to the electrode surface (diffusion-controlled). However, at the reduction (or oxidation) potential, the diffusion of the ions reaches its maximum because now the reaction is limited by the reaction's activation energy (activation-controlled). At this point, the current in the working electrode also reaches its

maximum (i_{pc} or i_{pa} in the CV plot in Figure 20b). As the potential scan continues, the current

starts to drop. This drop is because at these potentials the ions accumulate on the electrode
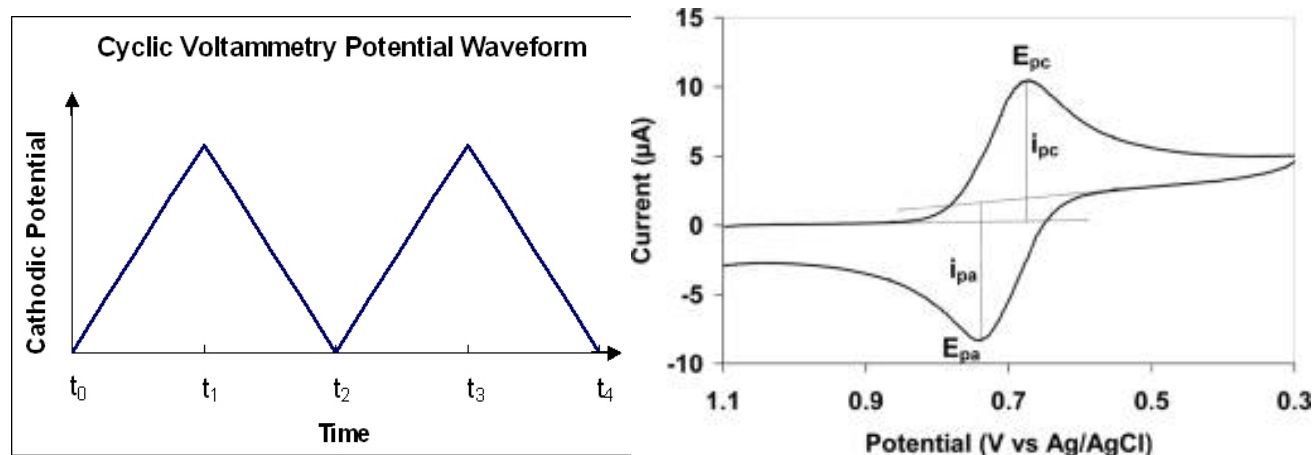
Figure 20 (a)Cyclic voltammetry waveform; (b) Typical cyclic voltammogram[52]

surface and do not reduced (or oxidized) fast enough.[53]

      In cyclic voltammetry, the peak current depends not only on the concentration and

diffusional properties of the electroactive species but also on scan rate. So, Randle-Sevcik

equation was commonly used to describes the effect of scan rate on the peak current ip.

$$i_p = 2.69 \cdot 10^5 n^{3/2} A D^{1/2} v^{1/2} \Delta C_0 \ (25 \ °C)$$

Where i_p is the peak current (mA), n is the number of electrons per reaction species, A is the

surface area of the electrode, D is the diffusion coefficient of Zn^{2+} (cm^2/s), v is the scan rate

(V/s), C_0 is the concentration change of zinc ions after reaction. By this equation, the zinc

diffusion coefficient of the hole system can be calculated. As the zinc diffusion rate in solution is

much higher than in cathode. So the result can be approximated to be the zinc diffusion

coefficient in cathode.

In this work, CV was tested on Bio-Logic VMP3 potentiostat with polished zinc foil as counter and reference electrode. Electrolyte is 2M ZnSO$_4$ with adjusted PH equals 4, and the voltage range is 0.8V to 2.0V.

2.2.3 Electrochemical Impedance Spectroscopy (EIS)

Electrochemical Impedance Spectroscopy (EIS) is a technique used to probe the response of a system to an electrical perturbation with varying frequency. Over a wide range of frequencies (i.e. 1 Hz to 1 MHz) various inductive and capacitive effects can be observed in a system. The electrochemical cell is exposed to a load at each frequency, the corresponding current flowing through the cell is measured, and software is used to deduce this value to its real and imaginary impedance components. There are two principal equations which describe the real and imaginary impedance components of EIS, shown in Equations 9 and 10, respectively, below:

$$Z' = R_s + \frac{R_{ct}}{1+\omega^2 R_{ct}^2 C_{dl}^2} \quad [9]$$

$$Z'' = \frac{R_{ct}^2 C_{dl}\omega}{1+\omega^2 R_{ct}^2 C_{dl}^2} \quad [10]$$

where Z' and Z'' are the real and imaginary components of impedance, R_s is the resistance of the electrolyte, R_{ct} is the charge transfer resistance, ω is the applied frequency, and C_{dl} is the capacitance of the double layer.

Figure 21 shows a typical Nyquist plot, which can be further broken down to its two main components: the activation-controlled region (represented by the semicircle) and the diffusion-controlled region (represented by the linear tail). Solution and charge transfer resistances are frequency independent and thus are both real quantities. Ion diffusivity is measured in the diffusion-controlled region and is observed at low frequencies. The inset in Figure 21 shows a simplified circuit used to model the experimental data.
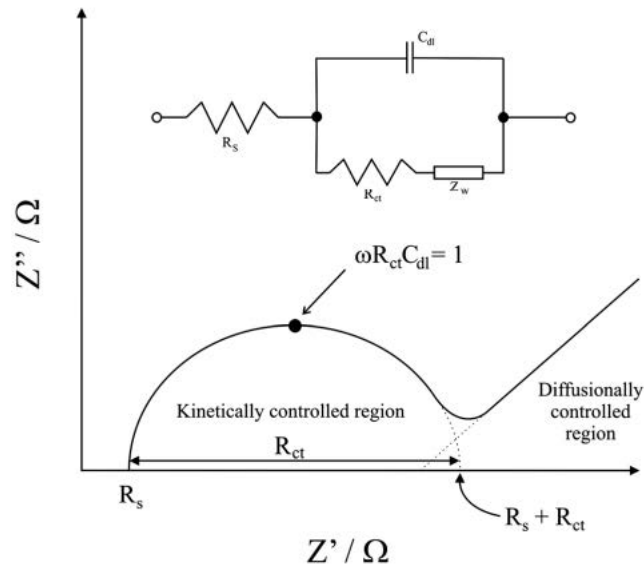
Figure 21 Typical Nyquist plot. Inset: simple Randles equivalent circuit for fitting EIS spectrum for an electrochemical cell[54]

In this project, EIS measurements were conducted on a Bio-Logic VMP3 electrochemical workstation with scanning of AC frequencies from 100 MHz to 10 mHz.

2.2.4 Battery Testing

Cycle life for coin (~ 1.15 cm^2 in 1.15 mAh cell) and large (~ 20.25 cm^2 in 7 mAh cell) cells were tested using the constant current (CC) protocol with voltage window between 0.8 V and 1.9 V vs. Zn^{2+}/Zn. In this mode, the cell is first charged to 1.9 V using the desired current rate, and discharge to 0.8V with the same current for one cycle.

To measure rate capability, the cycling C-rate was varied to observe the effect of current density on discharge capacity. Measurements were conducted at 50mA/g-100mA/g-200mA/g-500mA/g-1A/g-50mA/g using a constant current (CC) charge-discharge protocol.

Symmetric cell was tested in coin cell at a constant current density of $2mA \cdot cm^{-2}$ with one hour charge and discharge period, respectively. Symmetric cell in this project is used for studying the effect of G-AGM on dendrite inhibiting, so both cathode and anode side of the cell are zinc foil. The electrolyte used here is 2M zinc sulfate.

Chapter 3: Synthetization, Optimization and Characterization of Zinc Manganese Oxide Cathode

3.1 Synthesis of Cation Deficient Zinc Manganese Oxide with Different Cation Ratio

The cation deficient zinc manganese oxide was synthesized according to the previous report[17], but with small differences on the ratio of zinc nitrite and manganese nitrite. There are four types of ratio which are 50, 55, 60 and 65mL 0.2 M $Zn(NO3)2$ mixed with 100 mL 0.2 M $Mn(NO3)2$(cation ratio can be converted to 1:2, 1.1:2, 1.2:2, 1.3:2) and 1.6g carbon (graphite nanoplates (GNP), Zerocor Technologies) were pre-mixed and loaded into a 500 mL flask. 90 mL aqueous ammonia (28wt%) was prepared and constant dripped into the mixture in 1 hours with stirring. Then the mixture will be put into the oven for 3 hours under 180℃ to generate the product. The ZMO/C product was centrifuged at 2000RPM for 5 mins and washed by water and acetone separately for 3 times each. The final product contains about 80wt% of ZMO and 20wt% of carbon.

3.2 Cathode Fabrication and Battery Assembling

CR2032 coin-type batteries were employed for electrochemical tests. 90wt% ZMO/C composite as the mixture of active material and conductive agent, and 10wt% polyvinylidene fluoride (PVDF) as binding material were mixed in N-methyl pyrrolidinone (NMP) to form

slurry. The slurry was uniformly pasted onto a conductive polyethylene (PE) film (All-Spec 854-36150) with an active material mass loading of 4mg/cm^2 and vacuum dried at 80℃ for 4 hours.

A disk of 12mm diameter was cut to be the cathode. The electrolyte was 2M zinc sulfate blended with 0.1M manganese sulfate with the pH been adjusted to 4, and zinc foil was the anode. The manganese sulfate in the electrolyte is used for inhibiting manganese dissolution and improve initial capacity which have been proved by previous report.[21] The separator used in this project is Absorbed Glass Mat (AGM). Figure 22 illustrated the components of the coin cell.
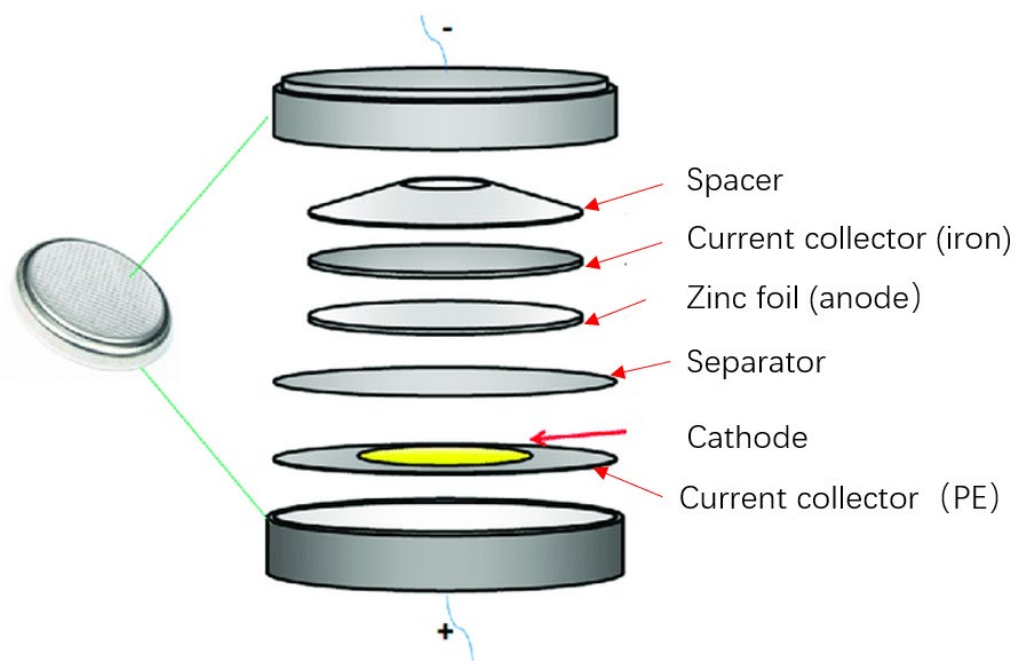
Figure 22 Schematic of the components of the coin cell

3.3 Material characterizations

TGA was done to quantify the percentage of carbon and zinc manganese oxide in the products respectively. As the figure 23 shows, all the products show a rapid decrease of weight at the temperature between 350℃ and 450℃, which is carbon combustion. After the carbon was combusted, the rest samples should be zinc manganese samples, and the percentage of the rest products are similar for all of four samples which are 75%, 78%, 79%, and 80% for the sample ZMO-1:2, ZMO-1.1:2, ZMO-1.2:2, and ZMO-1.3:2 respectively.
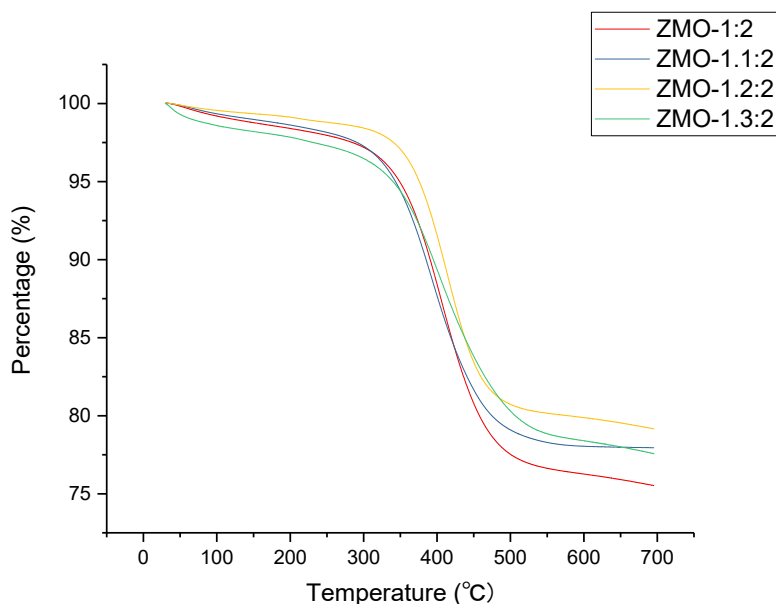
Figure 23 TGA of prepared ZMO/C composites

Figure 24 shows the morphology and topography of the prepared samples. The four samples are all well synthesized and uniformly distributed. There are some agglomerations of particles that can be observed, but most particles are around the size of 30nm.
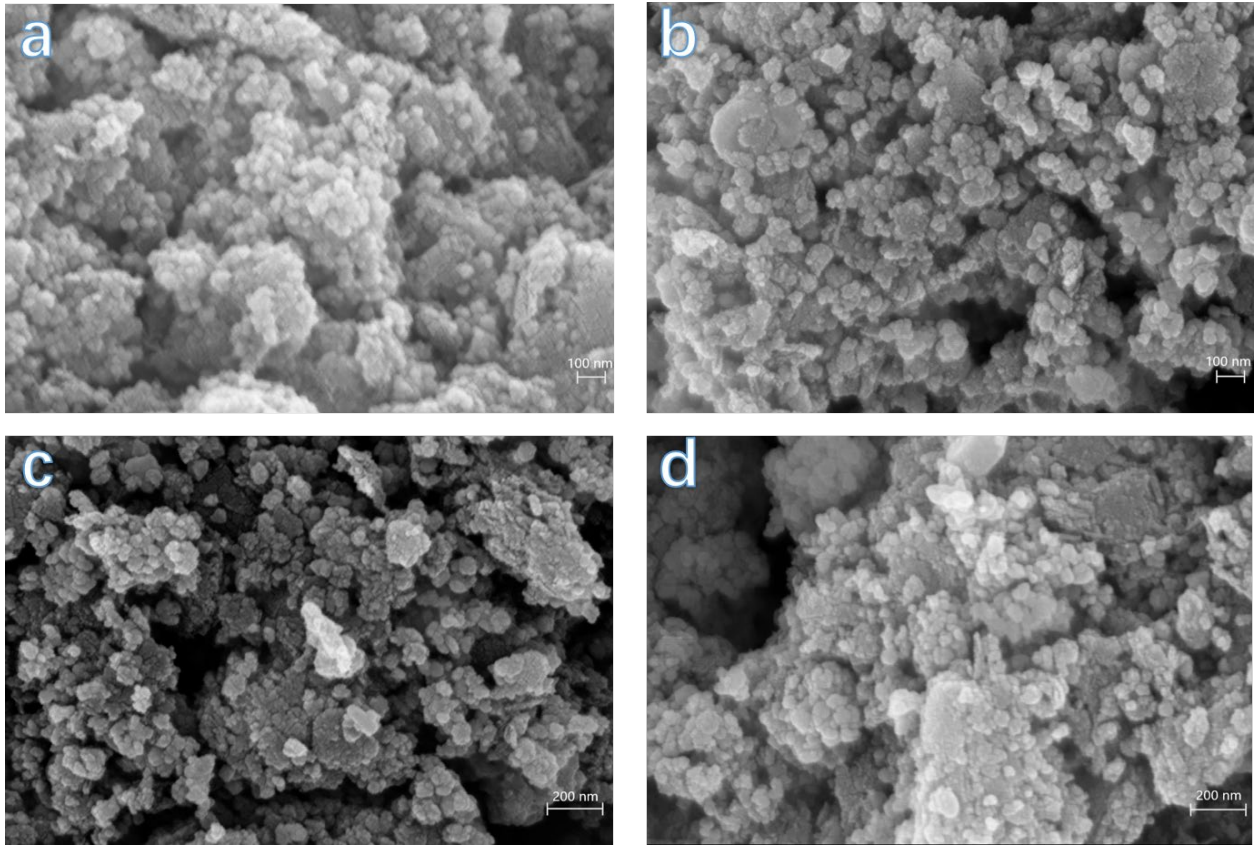
Figure 24 SEM images of (a) ZMO-1:2 sample; (b) ZMO-1.1:2 sample; (c) ZMO-1.2:2 sample; (d) ZMO-1.3:2 sample

Figure 25 is the XRD patterns of the synthesized samples, and all the samples have high crystallinity, which can be indicated by the high peak intensity. The patterns of the ZMO-1:2 and ZMO-1.1:2 samples are precisely the same and perfectly match the standard pattern of the body-centered tetragonal ZnMn2O4 (JCPDS no.24−1133). However, patterns of the sample ZMO-1.2:2 and ZMO-1.3:2 show other peaks which are readily assigned to the cubic zincblende structure ZnO (JCPDS no. 36-1451). The ZnO may come from the excess zinc cation during the synthesis.
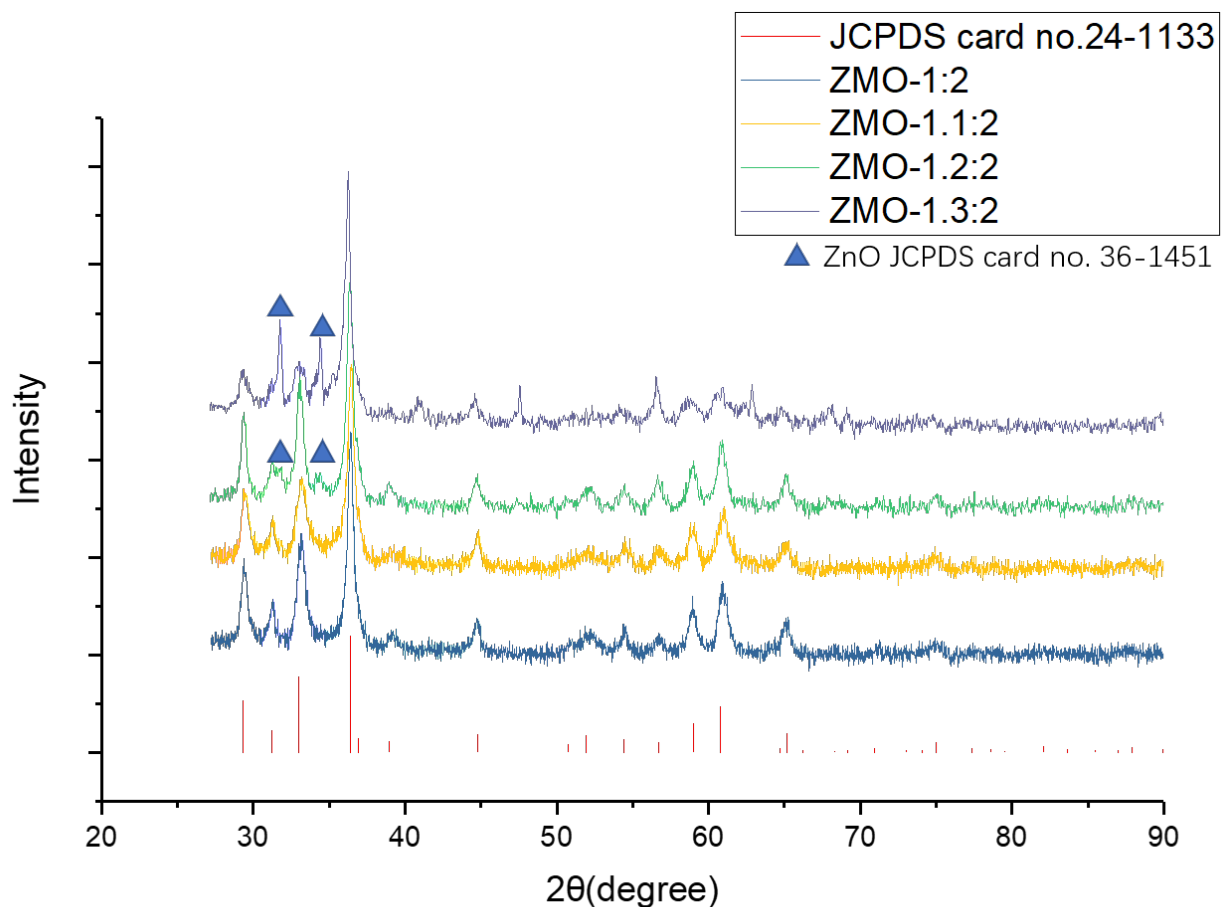
Figure 25 XRD patterns of the obtained samples

Figure 26 is the XPS spectrums include a full spectrum and high-resolution scans of the Mn2p peaks from all of the four samples. The survey spectra of the four samples are the same, which indicates the presence of zinc, manganese, oxide, and carbon elements. The two peaks with the binding energy of 642 eV and 654 eV are assigned to the Mn2p$_{3/2}$ and Mn2p$_{1/2}$, respectively.[55] Then, the spectra of high-resolution scans of Mn2p peaks are used for determining the percentage of Mn^{3+} and Mn^{4+} in the samples and then calculate the exactly Mn vacancies. The peak of Mn2p$_{3/2}$ can be split into two peaks which located at 641.2eV and 642.7eV in figure 26(b)-(e). These split peaks are due to the presence of Mn^{3+} and Mn^{4+}, where 641.2 eV is Mn^{3+} and 642.7 eV is Mn^{4+}

from literature.[56, 57] The similar results also show in the peak of Mn2p$_{1/2}$, where the split peaks located at 653.4eV and 653.9 eV, and these two binding energies also indicate the presence of Mn^{3+} and Mn^{4+}, respectively.[58, 59] The exact chemical sate percentage of Mn^{3+}, Mn^{4+} as well as the manganese vacancies can be seen in table 3.

Table 3 Fitting results from XPS spectra

	Percentage of Mn^{3+}	Percentage of Mn^{4+}	Exact Chemical Formula
ZMO-1.:2	73.4	26.6	ZnMn$_{1.84}$O$_4$
ZMO-1.1:2	59.8	40.2	ZnMn$_{1.76}$O$_4$
ZMO-1.2:2	53.2	46.8	ZnMn$_{1.73}$O$_4$
ZMO-1.3:2	48.5	51.5	ZnMn$_{1.71}$O$_4$

With the increasing amount of zinc cation during the synthesis, the percentage of Mn^{4+} increased which means an increasing amount of manganese vacancies. However, the increasing amount of manganese vacancies between the first two samples is 0.08, and it is much larger than the increasing amount between the last two samples which is only 0.02. It is due to the structure limitation; the amount of manganese cannot be increased unlimitedly.
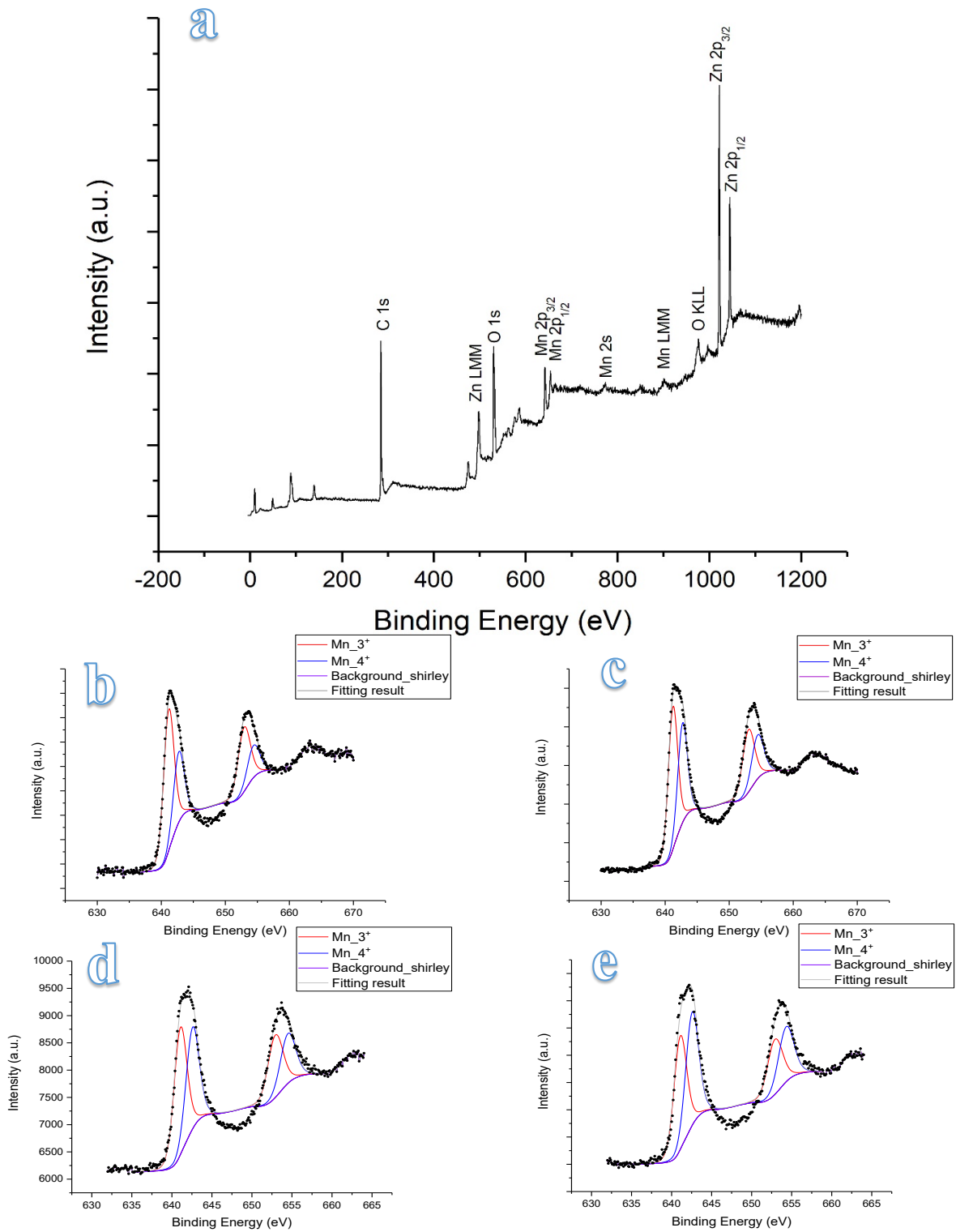
Figure 26 XPS spectra of the samples (a) survey spectrum; (b) Mn 2p spectrum of ZMO-1:2; (c) Mn 2p spectrum of ZMO-1.1:2; (d) Mn 2p spectrum of ZMO-1.2:2; (e) Mn 2p spectrum of ZMO-1.3:2

3.4 Electrochemical characterizations

The coin cells were assembled with the synthesized cathode material and tested. Figure 27 shows the battery performance of different cathode materials tested with $300mA \cdot g^{-1}$ current density. Firstly, the initial capacity increased by the increasing amount of manganese vacancies. The initial specific capacity of $ZnMn_{1.71}O_4$ is $170mAh \cdot g^{-1}$, which is 2.1 times larger compared with the initial capacity of $ZnMn_{1.84}O_4$ ($82mAh \cdot g^{-1}$). However, capacity retention shows the opposite trend, the $ZnMn_{1.71}O_4$ sample has the lowest capacity retention which is only 51.2%, and the capacity retention of $ZnMn_{1.84}O_4$ is 71.4%. The capacity fading may be caused by the manganese disproportionation reaction and dissolution. The more manganese vacancies exist, the more unstable structure it has, and finally cause more manganese dissolution and capacity fading.
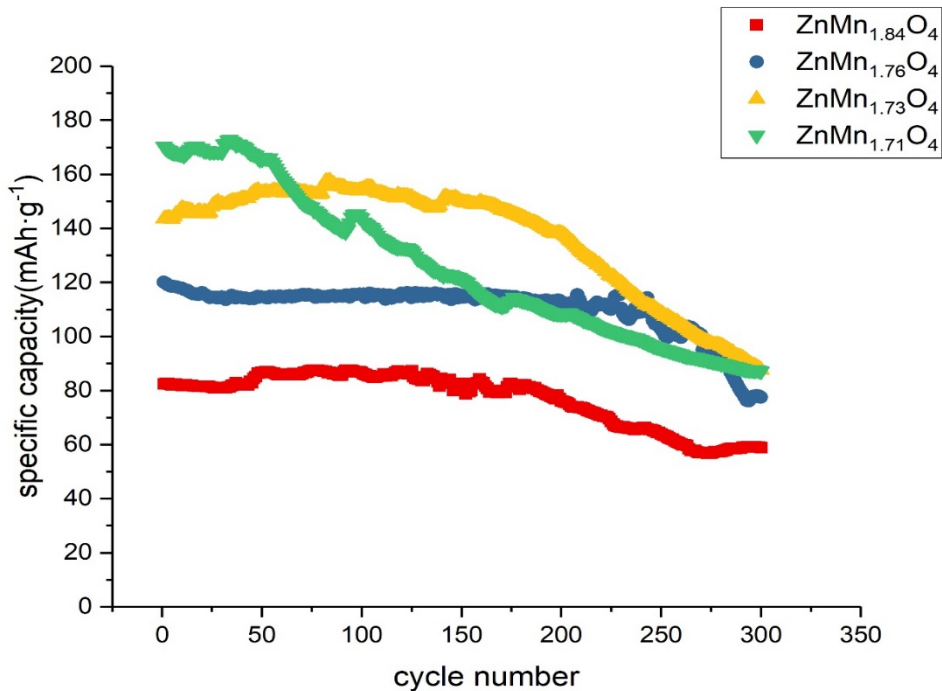
Figure 27 Batteries performance with different cathode materials

Figure 28 shows the cyclic voltammogram with different scan rates of different samples, respectively, and the relationships between the peak current and square root of scan rate in the main cathodic and anodic processes. Figure 28(a, c, e, f, g) show a similar result. Two separate peaks at 1.2V and 1.38 V can be clearly distinguished on the cathodic sweeping, and two overlapped peaks locate at 1.55V and 1.6V on the anodic seeping. These processes correspond to stepwise electrochemical Zn2+ insertion and extraction from the spinel structure which just like spinel $LiMn_2O_4$ cathode in LIBs.

The plots with the peak current and square root of scan rate can be used to calculate the zinc diffusion coefficient of the cathode material with the Randle-Sevcik equation:

$$i_p=2.69 \cdot 10^5 n^{3/2} A D^{1/2} v^{1/2} \Delta C_0 \text{ (25 °C) [11]}$$

	Zinc Diffusion Coefficient
$ZnMn_{1.84}O_4$	$2.43E\text{-}12 cm^2/s$
$ZnMn_{1.76}O_4$	$1.09E\text{-}11 cm^2/s$
$ZnMn_{1.73}O_4$	$3.20E\text{-}11 cm^2/s$
$ZnMn_{1.71}O_4$	$4.44E\text{-}11 cm^2/s$

Table 4 Zinc diffusion coefficient

Where i_p is the peak current (mA), n is the number of electrons per reaction species, A is the surface area of the electrode (with the geometric area of the electrode, $1.15cm^2$), D is the diffusion coefficient of Zn^{2+} (cm^2/s), v is the scan rate (V/s), C_0 is the concentration change of zinc ions after reaction. The calculated result can be seen in table 4. The zinc diffusion coefficient of $ZnMn_{1.71}O_4$ cathode is $4.44E-11cm^2/s$, which is comparable with the Li diffusion coefficient normally at a magnitude of $\sim 10^{-10}cm^2/s$ in spinel cathode.[60] However, the zinc
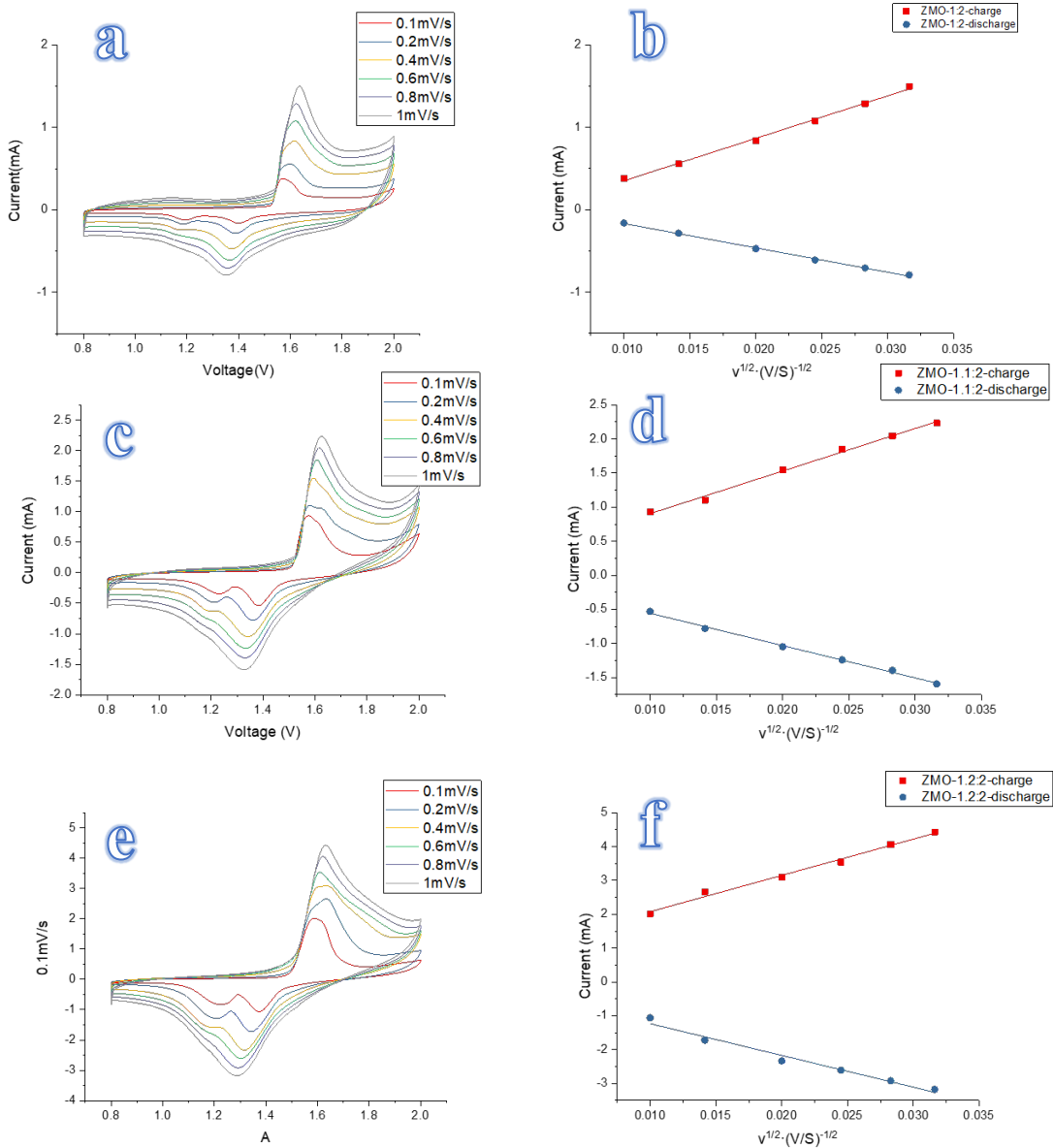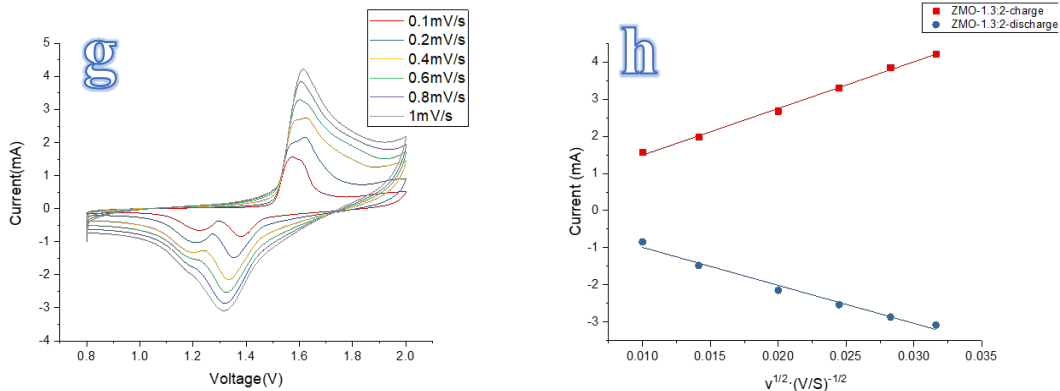
Figure 28(a, c, e, g) the cyclic voltammograms of samples at different scan rates; (b, d, f, h) the relationships between the peak current and square root of scan rate in the main cathodic and anodic processes

diffusivity of $ZnMn_{1.84}O_4$ is only 2.43E-12cm^2/s. As a result, the manganese vacancies in the spinel ZMO cathode have an effect to increase the zinc diffusivity.

The rate performance of the four cathode sample was also tested, and the results are presented in figure 29. The abnormally low capacity of the first cycle is due to the gradual activation of the electrode, similar to the observation from MnO2-based cathodes in ZIBs.[61] $ZnMn_{1.71}O_4$ cathode exhibit highest capacity at all current densities (average capacity of all current densities were calculated to be 219.8mAh·g^{-1}, 194.2 mAh·g^{-1}, 171.8 mAh·g^{-1}, 94.4 mAh·g^{-1}, 63.2 mAh·g^{-1}, 205.7 mAh·g^{-1}, respectively). Form the figure, the capacity difference is much apparent when the current density is low. However, the capacity difference decreased when the current density becomes large. Moreover, the reversibility of $ZnMn_{1.71}O_4$ cathode is the worst if compare the capacity of the first five cycles and the last five cycles.
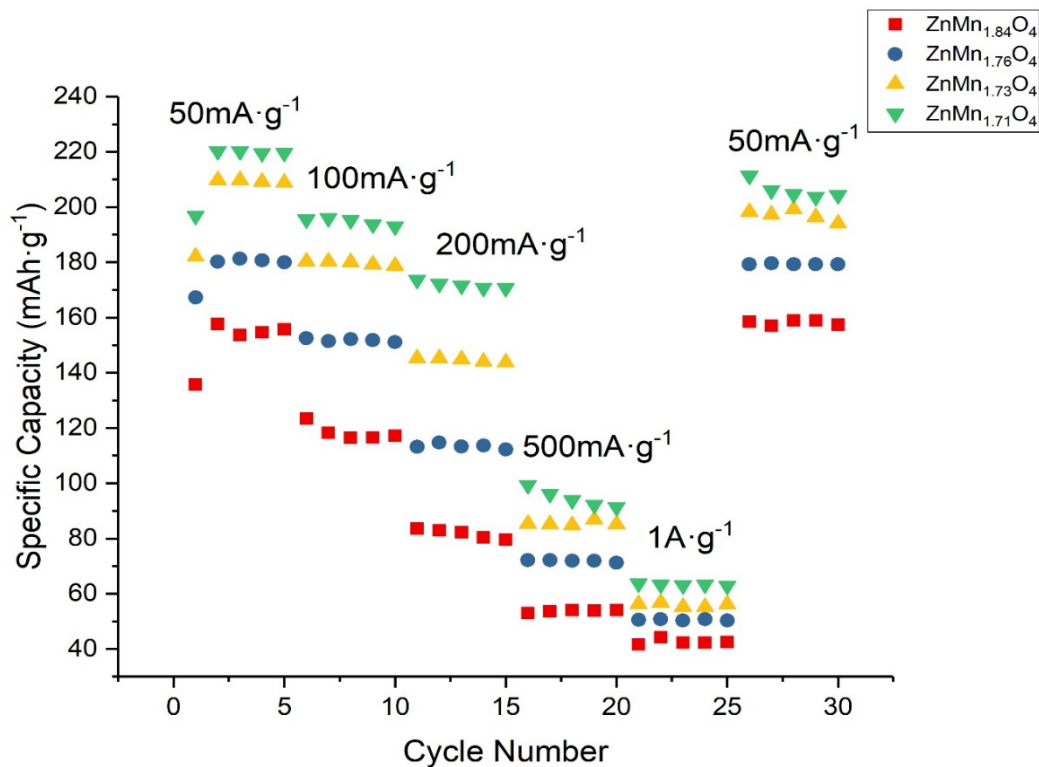
Figure 29 Specific capacity at different current densities of the four cathode samples

3.5 Conclusions

The cathode materials were successfully synthesized by an oxidation-precipitation process with different zinc and manganese cation with 78% of ZMO and 22% of carbon on average. Then, the number of manganese vacancies in the cathode materials were calculated by the XPS result. The goal of this project is successfully met as the initial specific capacity of $ZnMn_{1.71}O_4$ cathode achieves 220mAh·g^{-1} at 50mA·g^{-1} current density. The initial capacity of ZMO in the previous report is only 150mAh·g^{-1} at the same current density, which displays a 47% improvement.[17] Moreover, $ZnMn_{1.71}O_4$ cathode also has the best rate performance which the average capacity of all different densities was calculated to be 219.8mAh·g^{-1}, 194.2 mAh·g^{-1}, 171.8 mAh·g^{-1}, 94.4 mAh·g^{-1}, 63.2 mAh·g^{-1}, 205.7 mAh·g^{-1}, respectively. Furthermore, $ZnMn_{1.71}O_4$ cathode has the

44

highest zinc diffusivity ($4.44E-11cm^2/s$), which is even comparable with $LiMn_2O_4$ cathode in LIBs. The high zinc diffusivity is the fundamental reason for the high capacity and excellent rate performance.

Although the zinc diffusivity is increased significantly by the abundant of manganese vacancies, the structural stability is decreased dramatically. From the XRD result, all the cathode materials can perfectly match the standard ZMO pattern, but the sample $ZnMn_{1.73}O_4$ and $ZnMn_{1.71}O_4$ have some peaks corresponding to the zinc oxide. Moreover, the peaks of zinc oxide are more evident in the sample $ZnMn_{1.71}O_4$, and the crystallinity of $ZnMn_{1.71}O_4$ is also worse than other samples. The capacity retention of $ZnMn_{1.71}O_4$ cathode is only 51.2% after 300 cycles, which is much worse than the others (71.4%,64.5%, 61% respectively).

Overall, the initial capacity indeed increased by changing the cation ratio during the synthesis, but the structure stability decreased dramatically. The increased capacity comes from the change of zinc diffusivity of the cathode material. The capacity fading is due to the manganese disproportionation reaction and dissolution. Then, the next step is to try to stabilize the cathode and increase capacity retention.

Chapter 4: Fabrication, Optimization and Characterization of Gelatin Modified Separator

4.1 Fabrication and optimization of gelatin modified separator (G-AGM)

The gelatin modified AGM (g-AGM) was prepared by a straightforward method. The AGM was immersed into the 5wt% (Decided by the previous work in the group) gelatin solution for 1mins. Then the AGM was vacuum dried at 110 °C for 12 hours. A disk of 12mm diameter was cut to be the separator for the coin cell, which is as same as the coin cell in the previous section. Moreover, a 9cm2 square was cut to be the separator for the 7mAh to test capacity retention for long cycle life. Figure 30 is the picture of the 7mAh large battery which the mass loading (30mg) of the cathode is much close to the industrial standard. The cathode material used for this project is $ZnMn_{1.71}O_4$ which has been mentioned in the last section. The electrolyte is also as same as previous, which was 2M zinc sulfate blended with 0.1M manganese sulfate, and the pH was adjusted to 4. Zinc foil was the anode.
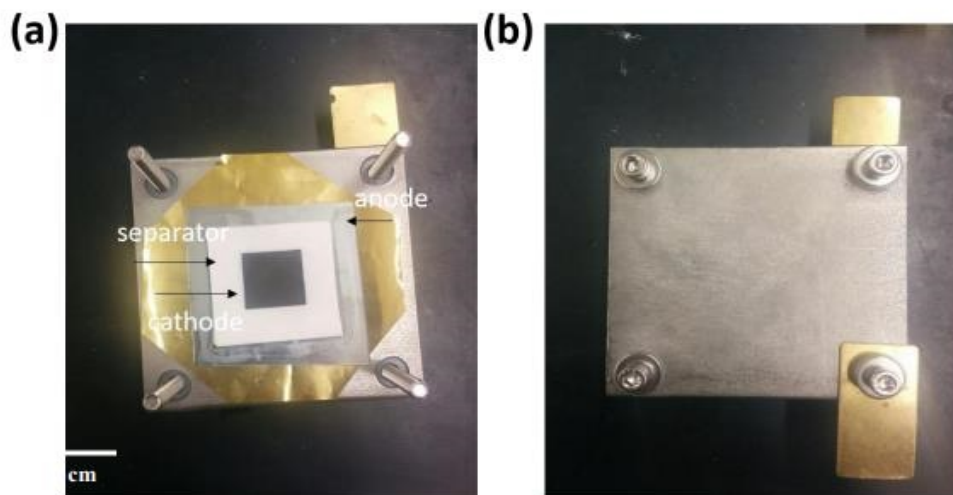
Figure 30 Picture showing (a) inner and (b) outer part of 7 mAh battery

4.2 basic Characterizations of G-AGM

Figure 31 is the SEM images of bare AGM and G-AGM. The bare AGM consist of glass fibers with the diameter in a range of 10nm-2μm. However, the gelatin in G-AGM is not particle form anymore, but becomes membrane connected with the fibers which can increase the toughness and mechanical strength of the separator.
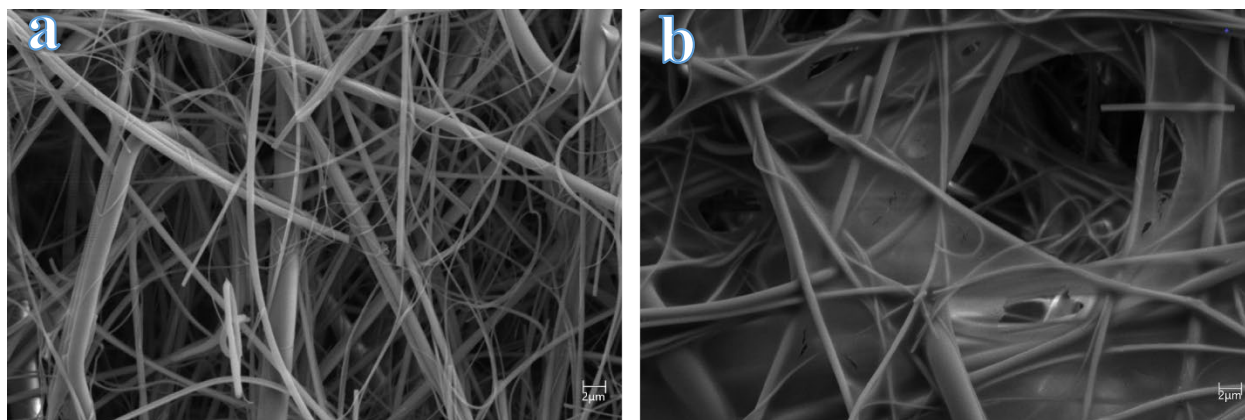
Figure 31 SEM image of (a) bare AGM; and (b) G-AGM

FTIR was also tested for comparing the bare AGM and G-AGM. The sharp peaks are located below 1000cm^{-1} which are all come from SiO$_2$ including Si-O-Si band and Si-O band due to the different bond vibration. The peak located at 1650cm^{-1} is corresponding to the peptide bond which comes from gelatin. Both SEM and FTIR can prove that gelatin is successfully attached to the AGM, and SEM images also indicate that gelatin transferred into membrane structure in the G-AGM.
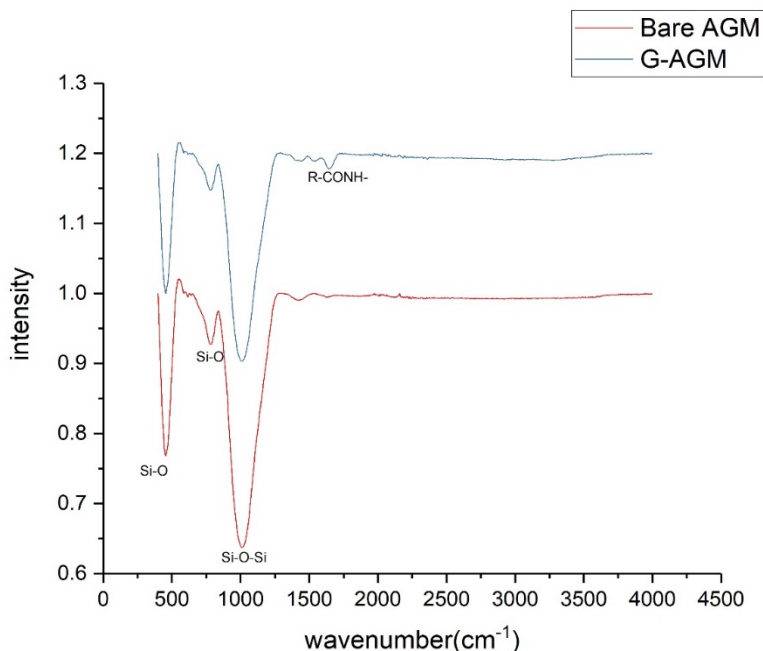
Figure 32 FTIR spectra of bare AGM and G-AGM

4.3 Battery Performance

Figure 33 shows the cycling performance of the coin cell with and without G-AGM tested at 300mA·g^{-1} current density and the cycling performance of the large battery with G-AGM at 500mA·g^{-1} current density. The coulombic efficiency is about 99%-100% for both samples in figure 33(a). Although the initial capacity of the batteries with g-AGM is only 103mAh/g which is much lower than the other samples, the capacity retention is after 500 cycles, the capacity retention achieves 91.3%. However, the capacity of the battery without G-AGM is only 57mAh·g^{-1} after 500 cycles with 33.5% capacity retention. G-AGM have great effect on prevent capacity fading, but the initial capacity decreased dramatically (the initial capacity of the battery without G-AGM is 170mAh·g^{-1}). The large battery was used for testing the capacity retention with high mass loading (30mg, and 4.8mg/cm^2) cathode in order to simulate the

industry situation. The initial capacity of the large battery at 500mA·g^{-1} current density is

62.7mAh·g^{-1}. After 2000 cycles, the capacity remains 80%, which is 50.2mAh·g^{-1}.
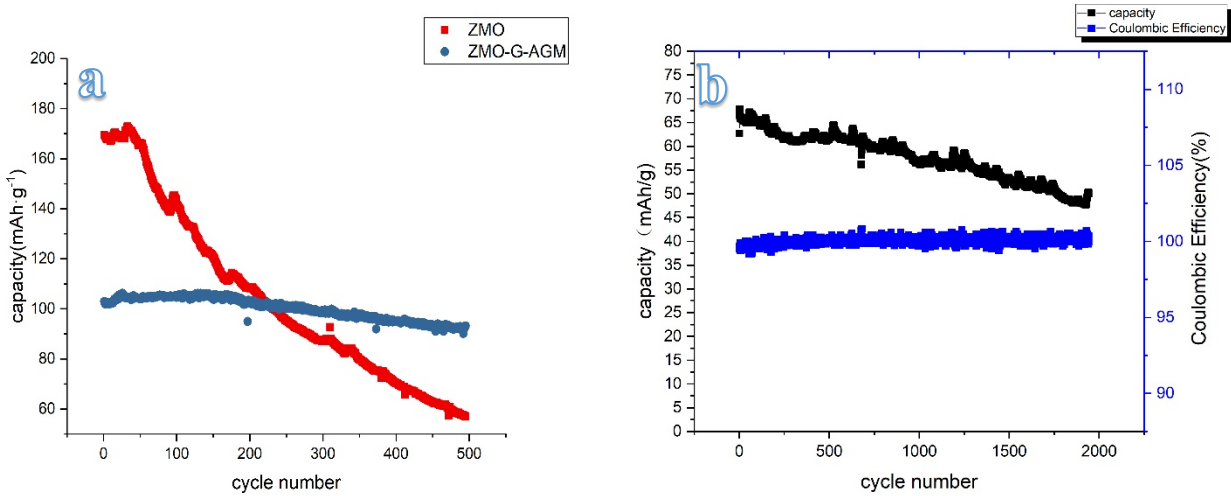
Figure 33 (a)Cycling performance of coin cell without G-AGM and with G-AGM; (b) cycling performance of 7mAh large battery with G-AGM

Figure 34 shows the rate performance of the coin cell with and without G-AGM. Notably, the capacities of both samples are the same (62mAh·g^{-1}) at 1A·g^{-1} current density. Moreover, the capacity difference between the two samples is small when the current density is 50mA·g^{-1} (220mAh·g^{-1} for the batteries without G-AGM, and 212mAh·g^{-1} for the batteries with G-AGM). When back to 50mA·g^{-1} in the last five cycles, the batteries with G-AGM exhibit better reversibility (97% retention, and 89%retention, respectively).
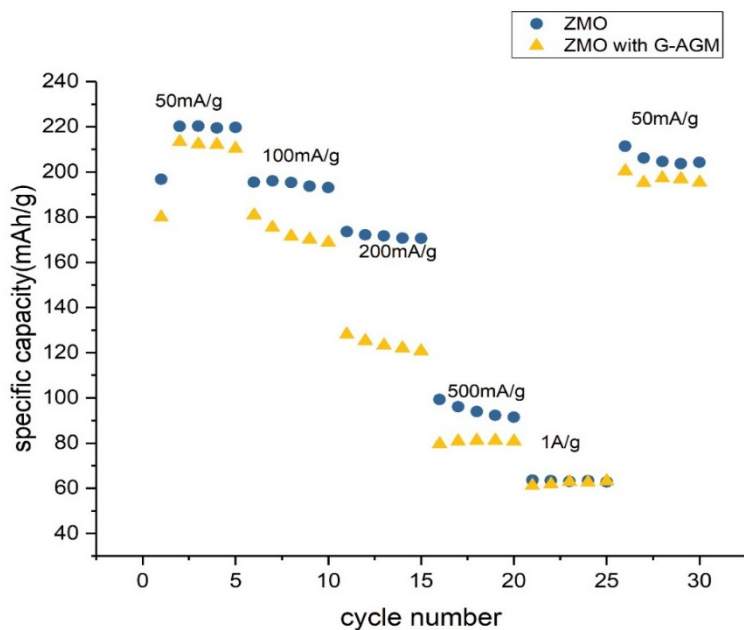
Figure 35 Rate performance of coin cell with and without G-AGM

Figure 35 is the charge-discharge profile of the coin cells with and without G-AGM separator for the first cycles at a current density of $50mA·g^{-1}$. The two plateaus observed in the charge-discharge profile correspond to the CV profile and are related to two stages of the Zn^{2+} extraction/insertion behavior in the cathode. However, the plateaus voltage of the batteries with G-AGM is larger than the other during the charging process, but the plateaus in the discharge process have the same voltage value.
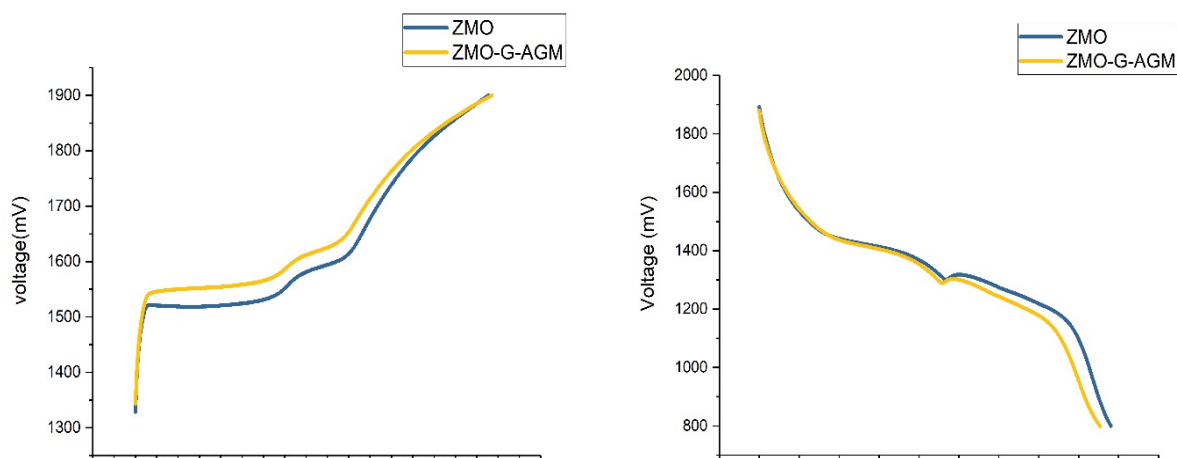
Figure 34 Charge-Discharge Curves

Figure 36 shows the result of the zinc to zinc symmetric cell test. The components of the zinc dendrite are not only zinc, but also include zinc hydroxide and zinc oxide.[29] So the voltage of the symmetric cell will increase if the zinc dendrite is formed along the surface of zinc foil. From the figure 36, the voltage of the cell without G-AGM increased dramatically from 2V to 5V (the limitation of the program is 5V) after about 3 days, which is due to the dendrite growth. However, the voltage of the cell with G-AGM is only 1V even after 5 days running which means uniformly electroplating and electrolysis during the charge and discharge.
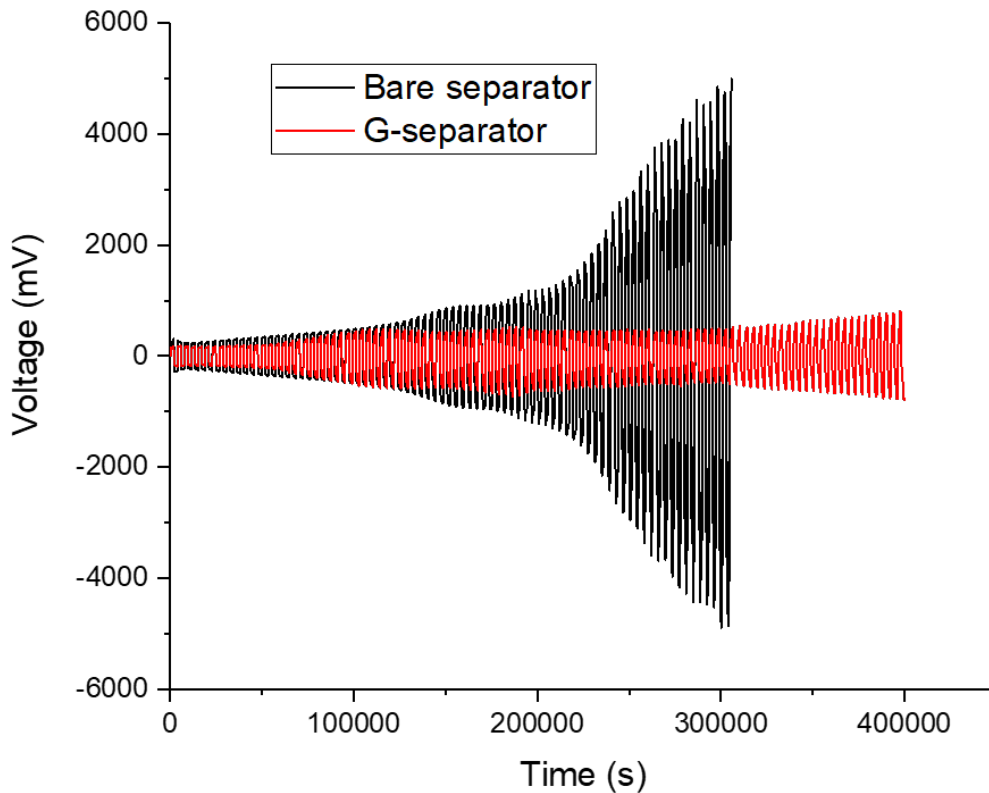
Figure 36 Zinc to zinc symmetric cell test with and without G-AGM separator for 5 days

4.4 Electrochemical and Material Characterizations

RD results of the cathode after charge and discharge are shown in figure 37(a). The signature peak of $Zn_4(OH)_6SO_4 \cdot 4H_2O$ is landed on the 8.52 degree of two theta, which also shown in the XRD pattern after discharge. While after charge, there is no peak corresponding to $Zn_4(OH)_6SO_4 \cdot 4H_2O$ anymore, but MnO_2 can be distinguished. Figure 37(b, c) are the SEM image of cathode after charge and discharge from the batteries without G-AGM. For the figure 37 (b), there are plenty of sheets can be seen on the surface of the cathode after discharge, which can be confirmed as zinc hydroxide sulfated. However, after charge, all the sheets are disappeared. From the previous report, the Mn^{3+} from $ZnMn_2O_4$ will have disproportionation reaction catalyzed by H^+ and dissolved into electrolyte (reaction 1). These processes will destroy the structure of the material, decrease the theoretical specific capacity and increase the PH. Furthermore, MnO_2 and Mn^{2+} can be mutually converted during the charge and discharge process (reaction 2). As a result, the more manganese ions dissolved, the higher PH value of the electrolyte will be detected after the discharge. When the PH reaches 5.47, zinc ions will be precipitated and form $Zn_4(OH)_6SO_4 \cdot 4H_2O$ (reaction 3).[16,62,63] The reactions are shown below:

$$ZnMn_2O_4 + 4H^+ \rightarrow MnO_2 + Mn^{2+} + Zn^{2+} + 2H_2O \quad \{1\}$$

$$MnO_2 + 4H^+ + 2e^- \rightleftarrows Mn^{2+} + 2H_2O \quad \{2\}$$

$$4Zn^{2+} + 6H_2O + SO_4^{2-} + 4H_2O \rightleftarrows Zn_4(OH)_6SO_4 \cdot 4H_2O + 6H^+ \quad \{3\}$$
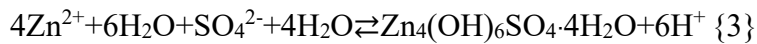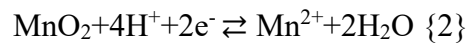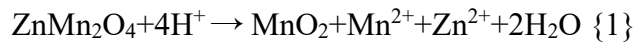
As a result, the lamellar zinc sulfate hydroxide was precipitated by the PH change which is induced by manganese disproportionation reaction and dissolution. Figure 37(d) shows the morphology of the cathode with G-AGM in the battery after charge. Compare with figure 37(b), the amount of zinc sulfate hydroxide is significantly decreased. Furthermore, the precipitates are distributed much smaller and uniform along the cathode surface. These results indicate that the gelatin has the ability to inhibit the manganese dissolution and maintain the spinel structure of the cathode during cycling.
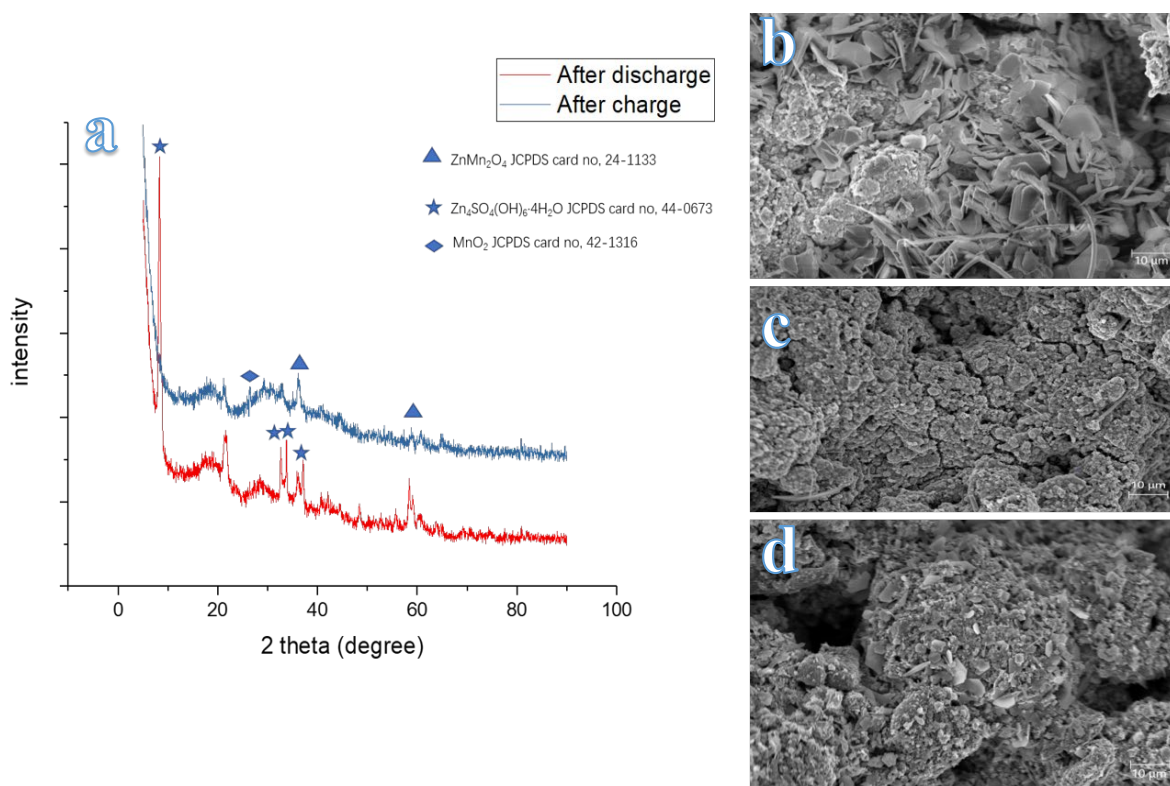
Figure 37 XRD pattern of the cathode after charge and discharge; SEM image of the cathode from the battery without G-AGM (b)after discharge, and (c) after charge; (d) SEM image of the cathode from the battery with G-AGM after discharge

Chronoamperometry (CA) was performed to study the dendrite formation and growth effected by G-AGM on the zinc anode. These tests were performed on a three-electrode system with zinc foil as a counter and working electrodes, and Ag/AgCl as a reference electrode, respectively, with over-potential of 120 mV for 1 hour. Figure 38 shows the results from CA test.

Compared the long-term chronoamperograms of zinc foil with and without G-AGM, the absolute current density was significantly lower after G-AGM was applied (3.14 mA·cm^{-2} for the G-AGM sample and 5.06 mA·cm^{-2} for the control sample). Moreover, overall increasement of the current density for the sample without G-AGM is 0.76mA·cm^{-2} after 1-hour chronoamperometry test, but the increasement of the current density for the sample with G-AGM is only 0.4 mA·cm^{-2}. From the chronoamperograms of the first ten seconds, it shows a quick drop in current density (current density dropped to 4.15 mA·cm^{-2} from 4.26 mA·cm^{-2} which only took 1.5s) initially which suggests fast nucleation of the zinc dendrites. Then the current Absolute current density increased along the time which is caused by an increase in surface area of the zinc anode. This increase in surface area is due to the dendritic zinc growth. However, the current density of the zinc anode with G-AGM also dropped at the initial, but took 4s, which is much longer than the control sample. Moreover, the current density remains plat after the drop which also indicates the dendrite growth was inhibited. All the results show that G-AGM have the ability to prevent zinc dendrite nucleation and growth.
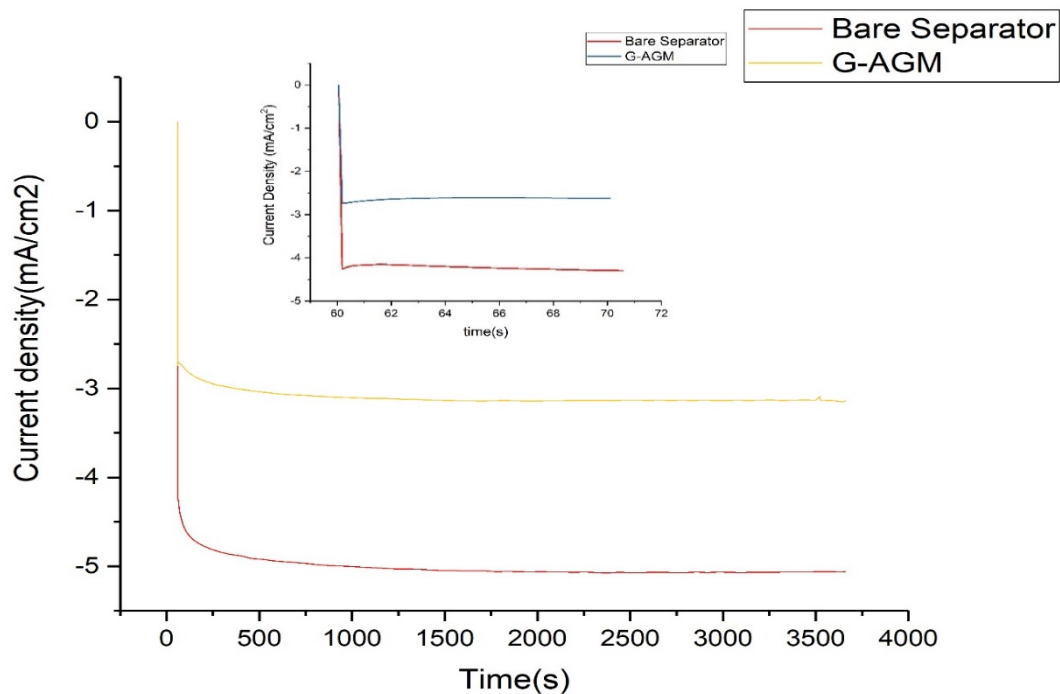
Figure 38 1-hour Chronoamperometry of zinc electrodes with and without G-AGM. Insert: first 10s of the chronoamperograms.

SEM images of zinc anodes with and without G-AGM after CA test is presented in Figure 39. The images evidently show the effect of G-AGM on anode side. The anode surface without G-AGM is filled with gravel-type dendrites with the diameter about few micrometers. After 10mins CA, the gravel-type dendrites growth and converted into strip like dendrite with much larger size. However, after 5 mins, the surface of the anode with G-AGM is uniformly distributed with small zinc nuclei. After 10 mins CA, mossy dendrites were observed on the surface.
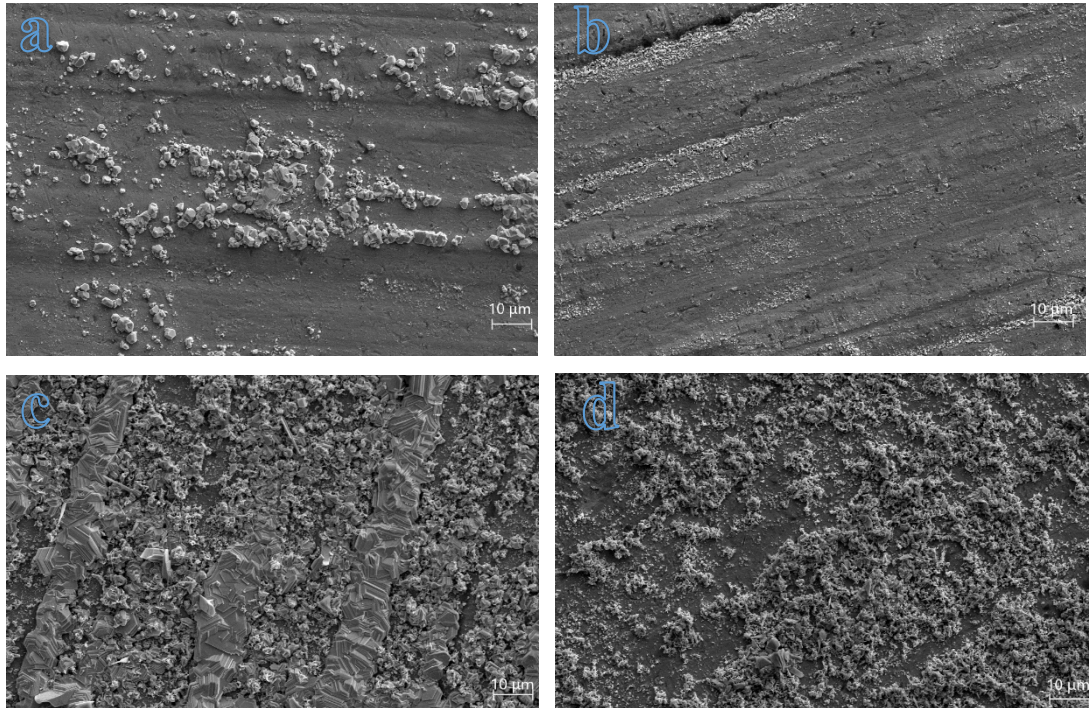
Figure 39 SEM image of zinc anode after 5 mins CA without G-AGM(a); with G-AGM(b); and SEM image of zinc anode after 10 mins CA without G-AGM(c); with G-AGM(d)

Figure 40 is the FTIR spectra of zinc electrodes after 10 mins CA, and pure zinc. The spectra of the counter electrode and pure zinc are almost the same. However, the spectrum of the working electrode shows 3 peaks located around 1000-1250 cm^{-1}. The two peaks located on 1025 and 1080cm^{-1} is corresponding to the OH bond from zinc hydroxide[64]. There is another peak located on 1230cm^{-1} which is corresponding to the gelatin[65]. The results can prove that gelatin can be absorbed on the zinc surface during the electroplating.
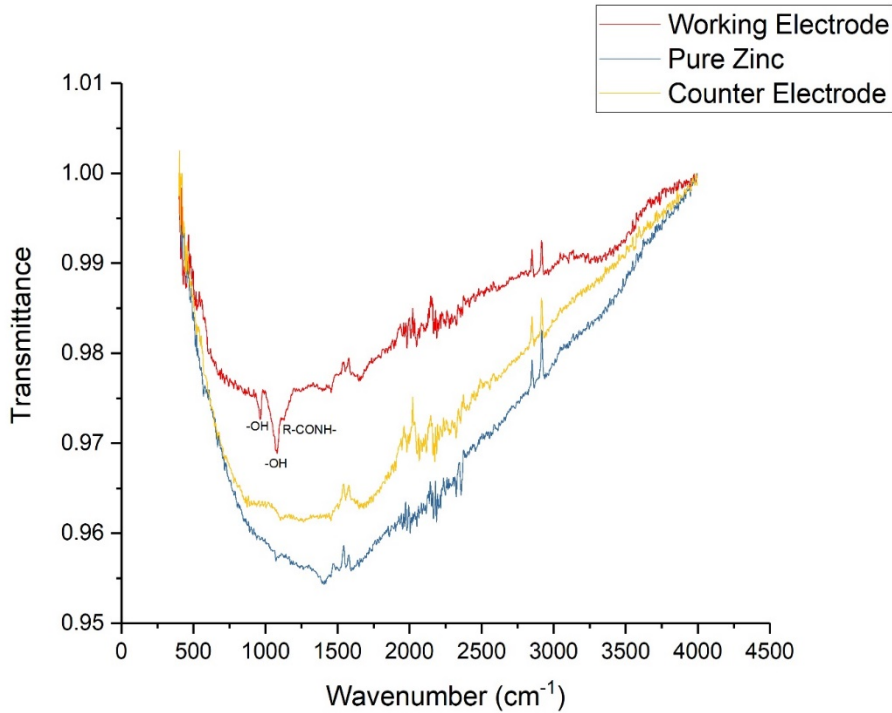
Figure 40 FTIR of zinc electrodes after 10 mins CA, and FTIR of pure zinc

Figure 41 shows the Nyquist plots of EIS measurements of the batteries with and without G-AGM, and the fitting results were presented in table 5. The Rs is negligible compare with Rct. The charge transfer resistance of the ZIBs without G-AGM is about 468.1Ω, but it increased to 897.7Ω when G-AGM was applied into the batteries. The dramatically increased Rct is due to the chelating effect of the gelatin[38]. If Zn^{2+} was chelated by gelatin, and become $ZnGl^+$. The charge decreased, but the molecular weight increased immensely. As a result, charge transfer resistant increased.

Table 5 Fitting results from the Nyquist plots

	Rs(ohm)	Rct(ohm)
ZMO	7.03	468.1
ZMO with G-AGM	14.7	897.7
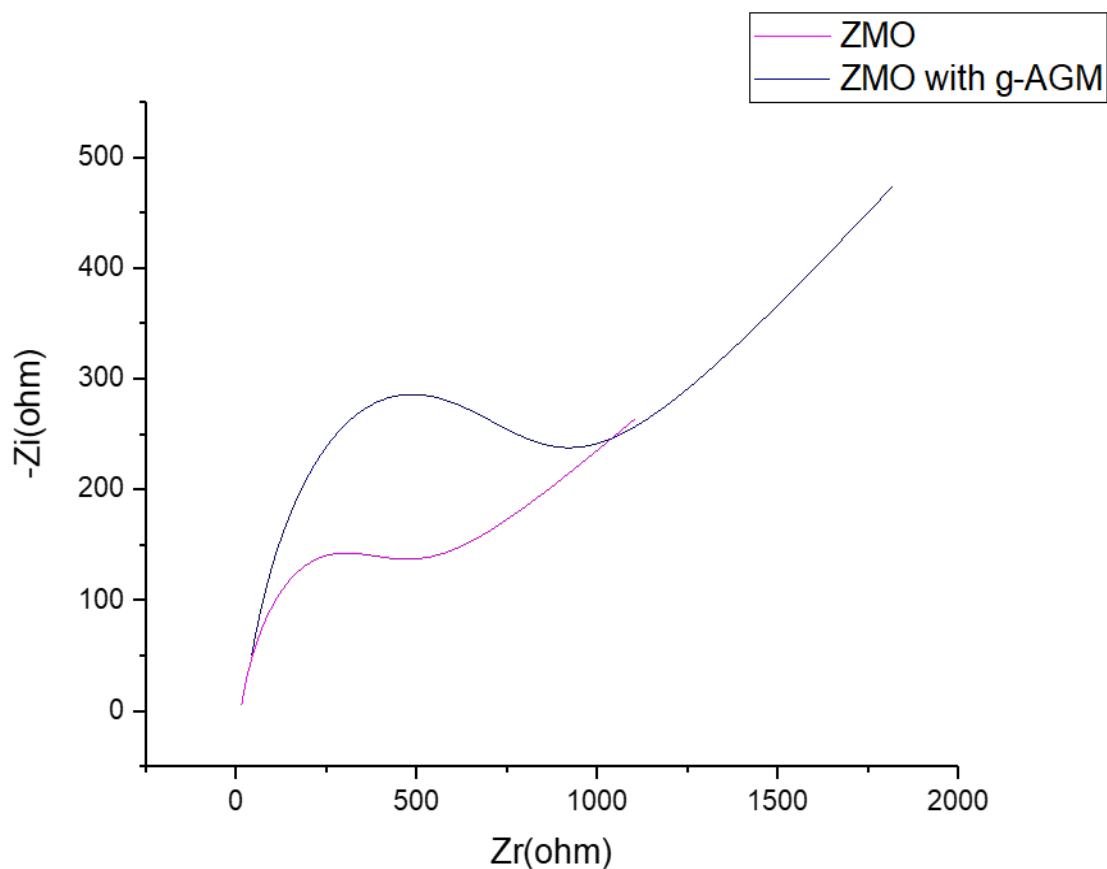
Figure 41 Nyquist plots of EIS measurements of the batteries with and without G-AGM.

4.5 Conclusions

Gelatin modified separator was fabricated successfully by a straightforward method. The gelatin transferred into membrane structure attached on the AGM that was found by the SEM images. The capacity retention of ZIBs are significantly improved after the G-AGM was applied. The capacity retention of the coin cell at the 300mA·g^{-1} current density achieves 91.3%, while only 33.5% of capacity remained for the batteries without G-AGM after 500 cycles. Moreover, 80% capacity remained after 2000cycles for the 7mAh large batteries with G-AGM. By the XRD

pattern and SEM images of the cathode after charge and discharge, G-AGM was found that it has the ability to inhibit the manganese disproportionation reaction and dissolution, and protect the spinel structure of the cathode material. Thereby, increase the capacity retention.

However, the initial capacity at the $300mA \cdot g^{-1}$ current density was decreased dramatically with G-AGM employed. From the rate performance results, G-AGM will affect the capacity especially in the current density range of $100mA \cdot g^{-1}$ to $500 mA \cdot g^{-1}$. However, when the current density is low like $50 mA \cdot g^{-1}$ or high enough ($>500 mA \cdot g^{-1}$), the capacity of the batteries with and without G-AGM are similar. High charge transfer resistance caused by G-AGM is the reason.

G-AGM also has the ability to inhibit the zinc dendrite formation. The zinc to zinc symmetric cell with G-AGM can run for 5 days without obvious voltage increasing. However, the voltage of the symmetric cell without G-AGM increased dramatically after 2 days' running. The increasing voltage is caused by the uncontrollable zinc dendrite growth. Chronoamperometry test also proves that the G-AGM have a great effect on inhibiting dendrite growth. Moreover, the speed of zinc dendrite nucleation also slowed down after G-AGM was introduced. SEM images of the zinc surface after CA with and without is the most direct evidence. FTIR spectra of zinc electrode after CA prove that gelatin will be adsorbed on the zinc surface during electroplating and form thin film. The gelatin film can cover the active sites on the working electrode, and decrease the nucleation rate, which finally, in turn, get a uniform coating without dendrite. [37, 39]

Chapter 5: Summary of the Thesis

Aqueous rechargeable zinc ion battery is an attractive candidate for next generation of battery energy storage system from the ecological, cost effective aspects thinking. However, there are only few cathode materials have been reported which can serve as the hosts of divalent Zn^{2+} ions including V_2O_5, MnO_2, Prussian blue analogues (PBAs) and $ZnMn_2O_4$. Nevertheless, all kinds of V2O5 nanostructure like nanowires and nanobelt are synthesized by hydrothermal method which means cannot be commercialized. [66] The various types of manganese-based cathode material (include ZMO and MnO_2) are suffering from the poor capacity retention due to the Mn dissolution via the disproportionation reaction.[67] Moreover, the anode undergoes detrimental oxidation and zinc dendritic growth during cycling is another problem for ARZIBs. With cycling, these dendrites grow taller, can pierce the separator along the way and ultimately make contact with the cathode. This contact leads to short-circuiting and ultimate failure of the battery. Furthermore, the initial capacity of ZMO in previous report is only 150 mAh·g^{-1} even use 3M zinc trifluoromethanesulfonate (Zn(CF3SO3)2) solution as electrolyte.

In this work, a stable ARZIBs based on ZMO cathode is reported. The cathode material was synthesized by oxidation-precipitation method. With increasing the zinc cation during the synthesize, ZMO with abundant manganese vacancies was obtained. The exact chemical formula of the ZMO with the most manganese vacancies is $ZnMn_{1.71}O_4$. Zinc diffusion coefficients of the cathode materials were calculated by the Randle-Sevcik equation. The $ZnMn_{1.71}O_4$ has the highest zinc diffusivity. Moreover, $ZnMn_{1.71}O_4$ cathode also has the highest initial capacity

(220mAh·g-1), which is close to the theoretical capacity (224 mAh·g^{-1}). The high zinc diffusivity and initial capacity are all promoted by the manganese vacancies. However, the abundant manganese vacancies make the cathode structure unstable. Thus, the capacity retention of the ZnMn$_{1.71}$O$_4$ is only 33.5% after 500 cycles.

Then, gelatin modified separator was introduced into the battery system to prolong the battery cycle life. The capacity retention achieves 91.3% after 500 cycles at the current density of 300mA·g^{-1}, which is an unimaginable improvement. Zinc to zinc symmetric cell was applied for simulating the dendrite growth during the cycling. The symmetric cell with G-AGM can keep ruing for five days without evident voltage increasing. However, the symmetric cells without G-AGM stop running on the third day due to the voltage is excess the limitation. The result of CA test and the SEM images of the zinc electrodes after CA test are all the evidence can prove that G-AGM has a strong effect on inhibiting zinc dendrite nucleation and growth.

Overall, A stable ARZIBs is obtained. The initial capacity is 212 mAh·g^{-1} at 50mA·g^{-1} current density, and 91.3% capacity retention after 500cycles operated in the current density of 300mA·g^{-1}. Large battery with high cathode material mass loading was also tested. The capacity is 80% after 2000 cycles with 500mA·g^{-1} current density.

References

(1)   International Renewable Energy Agency, "Insights on Renewables", 2019

  https://www.irena.org/

(2)   Windpower Engineering and Development, "Global energy storage market expected to reach 22.2 GW in 2023, finds GlobalData", 2019 https://www.windpowerengineering.com/business-news-projects/global-energy-storage-market-expected-to-reach-22-2-gw-in-2023-finds-globaldata/

(3)   Global Data, "Power Intelligence Center", 2018

(4)   Recharge, "Recharge market data 2019", 2019 https://www.rechargebatteries.org/wp-content/uploads/2019/05/RECHARGE-Market-Data-2019.pdf

(5)   X. Wu et al., "The electrochemical performance improvement of LiMn2O4/Zn based on zinc foil as the current collector and thiourea as an electrolyte additive," J. Power Sources, vol. 300, pp. 453–459, Dec. 2015.

(6)   Battlebury, D. (1999). A high-performance lead–acid battery for EV applications. Journal of Power Sources, 80(1), 7-11.

(7)   G. Majeau-Bettez, T. R. Hawkins, and A. Hammer Strømman, "Life Cycle Environmental Assessment of Lithium-Ion and Nickel Metal Hydride Batteries for Plug-In Hybrid and Battery Electric Vehicles," Environ. Sci. Technol, vol. 45, pp. 4548–4554, 2011.

(8)   Zhou, X., Young, K., West, J., Regalado, J., & Cherisol, K. (2013). Degradation mechanisms of high-energy bipolar nickel metal hydride battery with AB.sub.5 and A.sub.2B.sub.7 alloys. Journal of Alloys and Compounds, 580, S373-S377.

(9)   Luo, J., & Xia, Y. (2007). Aqueous Lithium-ion Battery LiTi 2 (PO 4) 3 /LiMn 2 O 4 with High Power and Energy Densities as well as Superior Cycling Stability**. Advanced Functional Materials, 17(18), 3877-3884.

(10)   Saw, Ye, & Tay. (2016). Integration issues of lithium-ion battery into electric vehicles battery pack. Journal of Cleaner Production, 113, 1032-1045.

(11)   Kim, H, Hong, J, Park, Ky, Kim, Sw, & Kang, K. (2014). Aqueous Rechargeable Li and Na Ion Batteries. Chemical Reviews, 114(23), 11788-11827.

(12)   Z. Chang et al., "A lithium ion battery using an aqueous electrolyte solution," Sci. Rep., vol. 6, no. 1, p. 28421, Sep. 2016.

(13)   Liu, Jun, Hu, Junping, Deng, Qi, Mo, Jun, Xie, Hao, Liu, Zaichun, . . . Wu, Yuping. (2015). Aqueous Rechargeable Batteries for Large-scale Energy Storage. Israel Journal of Chemistry, 55(5), 521-536.

(14)   Li, W., Dahn, J., & Wainwright, D. (1994). Rechargeable Lithium Batteries with Aqueous Electrolytes. Science, 264(5162), 1115-1118.

(15)   Liu, Xu, Chen, Ni, & Shen. (2018). Progress in aqueous rechargeable batteries. Green Energy and Environment, 3(1), 20-41.

(16)   Zhang, Ning, Cheng, Fangyi, Liu, Yongchang, Zhao, Qing, Lei, Kaixiang, Chen, Chengcheng, . . . Chen, Jun. (2016). Cation-Deficient Spinel ZnMnO Cathode in Zn(CF3SO3)2 Electrolyte for Rechargeable Aqueous Zn-Ion Battery. Journal of the American Chemical Society, 138(39), 12894-12901.

(17)   Chun Li, Xiaopeng Han, Fangyi Cheng, Yuxiang Hu, Chengcheng Chen, & Jun Chen. (2015). Phase and composition controllable synthesis of cobalt manganese spinel nanoparticles towards efficient oxygen electrocatalysis. Nature Communications, 6, Nature Communications, 2015, Vol.6.

(18)   Alves, R., Rodrigues, L., Andrade, J., Fernandes, M., Pinto, J., Pereira, L., . . . Silva, M. (2013). Gelatin$_n$ Zn(CF$_3$SO$_3$)$_2$ Polymer Electrolytes for Electrochromic Devices. Electroanalysis, 25(6), 1483-1490.

(19)   Xiao, X., Ahn, D., Liu, Z., Kim, J., & Lu, P. (2013). Atomic layer coating to mitigate capacity fading associated with manganese dissolution in lithium ion batteries. Electrochemistry Communications, 32, 31-34.

(20)   Alfaruqi, Muhammad Hilmy, Islam, Saiful, Putro, Dimas Yunianto, Mathew, Vinod, Kim, Sungjin, Jo, Jeonggeun, . . . Kim, Jaekook. (2018). Structural transformation and electrochemical study of layered MnO2 in rechargeable aqueous zinc-ion battery. Electrochimica Acta, 276, 1-11.

(21)   Wu, Xianwen, Xiang, Yanhong, Peng, Qingjing, Wu, Xiangsi, Li, Yehua, Tang, Fang, . . . Wu, Xianming. (2017). Green-low-cost rechargeable aqueous zinc-ion batteries using hollow porous spinel ZnMn 2 O 4 as the cathode material. Journal of Materials Chemistry A, 5(34), 17990-17997.

(22)   Jang, D. H., Shin, Y. J., & Oh, S. M. (1996). Dissolution of spinel oxides and capacity losses in 4 V Li/Li x Mn 2 O 4 cells. Journal of the Electrochemical Society, 143(7), 2204-2211.

(23)   C. A. Loto, "Electrodeposition of Zinc from Acid Based Solutions: A Review and Experimental Study," Asian J. Appl. Sci., vol. 5, no. 6, pp. 314–326, Jun. 2012.

(24)   S. Higashi, S. W. Lee, J. S. Lee, K. Takechi, and Y. Cui, "Avoiding short circuits from zinc metal dendrites in anode by backside-plating configuration," Nat. Commun., vol. 7, p. 11801, Jun. 2016.

(25)   Walz, Johnson, Genthe, Stoiber, Zeltner, Anderson, & Thackeray. (2010). Elevated temperature cycling stability and electrochemical impedance of LiMn 2O 4 cathodes with nanoporous ZrO 2 and TiO 2 coatings. Journal of Power Sources, 195(15), 4943-4951.

(26)   Huilin Pan, Yuyan Shao, Pengfei Yan, Yingwen Cheng, Kee Sung Han, Zimin Nie, . . . Jun Liu. (2016). Reversible aqueous zinc/manganese oxide energy storage from conversion reactions. Nature Energy, 1(5), Nature Energy, 2016.

(27)   J.S. Ko, M.B. Sassin, J.F. Parker, D.R. Rolison, J. Long, Combining battery-like and pseudocapacitive charge storage in 3D MnOx@carbon electrode architectures for zinc-ion cells, Sustain. Energy Fuel. 2 (2018) 626e636.

(28)   Lu, W., Xie, C., Zhang, H., & Li, X. (2018). Inhibition of Zinc Dendrite Growth in Zinc-Based Batteries. ChemSusChem, 11(23), 3996-4006.

(29)   A. Mitha, A. Z. Yazdi, M. Ahmed, and P. Chen, "Surface Adsorption of Polyethylene Glycol to Suppress Dendrite Formation on Zinc Anodes in Rechargeable Aqueous Batteries," ChemElectroChem, Jun. 2018.

(30)   Ahmed, M., Yazdi, A., Mitha, A., & Chen, P. (2018). Introducing Artificial Solid Electrolyte Interphase onto the Anode of Aqueous Lithium Energy Storage Systems. ACS Applied Materials & Interfaces, 10(36), 30348-30356.

(31)   T. K. A. Hoang, M. Acton, H. T. H. Chen, Y. Huang, T. N. L. Doan, and P. Chen, "Sustainable gel electrolyte containing Pb2+as corrosion inhibitor and dendrite suppressor for the zinc anode in the rechargeable hybrid aqueous battery," Mater. Today Energy, 2017.

(32)   Yamada, Yuki, Furukawa, Keizo, Sodeyama, Keitaro, Kikuchi, Keisuke, Yaegashi, Makoto, Tateyama, Yoshitaka, & Yamada, Atsuo. (2014). Unusual stability of acetonitrile-based superconcentrated electrolytes for fast-charging lithium-ion batteries. Journal of the American Chemical Society, 136(13), 5039-5046.

(33)   Mcbreen, & Gannon. (1981). The electrochemistry of metal oxide additives in pasted zinc electrodes. Electrochimica Acta, 26(10), 1439-1446.

(34)   M. Shayegan, N. Rezaei, N. H. Lam, T. Altindal. (2013) "Probing multiscale mechanics of collagen with optical tweezers", SPIE Proceedings Vol. 8810.

(35)   Hugahoody, Pie chart displaying the Amino Acid composition in Gelatin. 2011.

(36)   A.G. Betts Electrochem. Ind., 1 (1903), p. 407

(37)   Meudre, Ricq, Hihn, Moutarlier, Monnin, & Heintz. (2014). Adsorption of gelatin during electrodeposition of copper and tin–copper alloys from acid sulfate electrolyte. Surface & Coatings Technology, 252, 93-101.

(38)   Ballesteros, Chaînet, Ozil, Trejo, & Meas. (2010). Initial stages of the electrocrystallization of copper from non-cyanide alkaline bath containing glycine. Journal of Electroanalytical Chemistry, 645(2), 94-102.

(39)   Alvarez, & Salinas. (2004). Nucleation and growth of Zn on HOPG in the presence of gelatine as additive. Journal of Electroanalytical Chemistry, 566(2), 393-400.

(40)   Wen, & Szpunar. (2005). Nucleation and growth of tin on low carbon steel. Electrochimica Acta, 50(12), 2393-2399.

(41)   Goh, Haseeb, & Sabri. (2012). Effects of hydroquinone and gelatin on the electrodeposition of Sn–Bi low temperature Pb-free solder. Electrochimica Acta, 90(C), 265-273.

(42)   Li, Hongfei, Han, Cuiping, Huang, Yan, Huang, Yang, Zhu, Minshen, Pei, Zengxia, . . . Zhi, Chunyi. (2018). An extremely safe and wearable solid-state zinc ion battery based on a hierarchical structured polymer electrolyte. Energy & Environmental Science, 11(4), 941-951.

(43)   Nanoimages, "SEM Technology Overview – Scanning Electron Microscopy", 2019. Retrieved from: https://www.nanoimages.com/sem-technology-overview/

(44)   Energy.gov, "Portable Parallel Beam X-Ray Diffraction System" Retrieved from: https://www.energy.gov/eere/amo/portable-parallel-beam-x-ray-diffraction-system

(45)   Langford, J. I.; Wilson, A. J. C.; IUCr. Scherrer after Sixty Years: A Survey and Some New Results in the Determination of Crystallite Size. J. Appl. Crystallogr. 1978, 11 (2), 102–113.

(46)   Sanchonx, "Interferometer for FTIR", 2011, Wikipedia. Retrieved from: https://en.wikipedia.org/wiki/File:FTIR_Interferometer.png

(47)   NETZSCH Website, "Thermogravimetric Analysis (TGA)". Retrieved from: https://www.netzsch-thermal-academy.com/en/advanced-materials-testing/methods/thermogravimetric-analysis/

(48)   Bvcrist, "X-Ray Photoelectron Spectroscopy", 2009, Wikipedia. Retrieved from: https://en.wikipedia.org/wiki/File:System2.gif.

(49)   "What is X-Ray Photoelectron Spectroscopy (XPS)?", Thermo scientific. Retrieved from: https://xpssimplified.com/whatisxps.php.

(50)   Grayyang, "Chronoamperometry", 2018, Wikipedia. Retrieved from: https://en.wikipedia.org/wiki/File:Scheme_of_chronoamperometry_instrument.png

(51)   Grujicic, & Pesic. (2002). Electrodeposition of copper: The nucleation mechanisms. Electrochimica Acta, 47(18), 2901-2912.

(52)   "Cyclic voltammetry" 2019, Wikipedia. Retrieved from: https://en.wikipedia.org/wiki/Cyclic_voltammetry

(53)   N. Elgrishi, K. J. Rountree, B. D. Mccarthy, E. S. Rountree, T. T. Eisenhart, and J. L. Dempsey, "A Practical Beginner's Guide to Cyclic Voltammetry."

(54)   Macdonald, D. D. Reflections on the History of Electrochemical Impedance Spectroscopy. Electrochim. Acta 2006, 51 (8–9), 1376–1388.

(55)   Feng, Z., Chen, X., Qiao, L., Lipson, A., Fister, T., Zeng, L., . . . Fenter, P. (2015). Phase-Controlled Electrochemical Activity of Epitaxial Mg-Spinel Thin Films. ACS Applied Materials & Interfaces, 7(51), 28438-28443.

(56)   Oku M., Hirokawa K., Ikeda S. J. Electron Spectrosc. Relat. Phenom. 7, 465 (1975)

(57)   DiCastro V., Polzonetti G., Contini G., Cozza C., Paponetti B. Surf. Interface Anal. 16, 571 (1990)

(58)   Allen G.C., Harris S.J, Jutson J.A., Dyke J.M. Appl. Surf. Sci. 37, 111 (1989)

(59)   Tan B.J., Klabunde K.J., Sherwood P.M.A. J. Am. Chem. Soc. 113, 855 (1991)

(60)   Linden, D.; Reddy, T. Handbook of Batteries, 3rd ed.; McGraw-Hill: New York, 2002.

(61)   Alfaruqi, Muhammad H., Mathew, Vinod, Gim, Jihyeon, Kim, Sungjin, Song, Jinju, Baboo, Joseph P., . . . Kim, Jaekook. (2015). Electrochemically Induced Structural Transformation in a γ-MnO 2 Cathode of a High Capacity Zinc-Ion Battery System. Chemistry of Materials, 27(10), 3609-3620.

(62)   Lee, Boeun, Seo, Hyo Ree, Lee, Hae Ri, Yoon, Chong Seung, Kim, Jong Hak, Chung, Kyung Yoon, . . . Oh, Si Hyoung. (2016). Critical Role of pH Evolution of Electrolyte in the Reaction Mechanism for Rechargeable Zinc Batteries. ChemSusChem, 9(20), 2948-2956.

(63)   Pan, H., Shao, Y., Yan, P., Cheng, Y., Han, K., Nie, Z., . . . Liu, J. (2016). Reversible aqueous zinc/manganese oxide energy storage from conversion reactions. Nature Energy, 1, Nature Energy, 2016 Apr 18, Vol.1.

(64)   Srivastava, O., & Secco, E. (1967). Studies on metal hydroxy compounds. II. Infrared spectra of zinc derivatives -Zn(OH) 2 , -ZnOHCl, ZnOHF, Zn 5 (OH) 8 Cl 2 , and Zn 5 (OH) 8 Cl 2 H 2 O. Canadian Journal of Chemistry, 45(6), 585-588.

(65)   Muyonga, Cole, & Duodu. (2004). Fourier transform infrared (FTIR) spectroscopic study of acid soluble collagen and gelatin from skins and bones of young and adult Nile perch (Lates niloticus). Food Chemistry, 86(3), 325-332.

(66)   Kundu, D. D., Adams, B. H., Duffort, V. F., Vajargah, S., & Nazar, L. (2016). A high-capacity and long-life aqueous rechargeable zinc battery using a metal oxide intercalation cathode. Nature Energy, 1(10), 16119.

(67)   L. Y. Zhang, L. Chen, X. F. Zhou and Z. P. Liu, Sci. Rep., 2015, 5, 18263.